Ecohydrological Model for Grassland Lacking Historical Measurements I: Downscaling Evaporation Data Based on Dynamic Sensitive Parameters and Deep Learning

Mingyang Li[1], Tingxi Liu[1*], Limin Duan[1], Long Ma[1], Yixuan Wang[1], Guoqiang Wang[2], Huimin Lei[3], Qiusheng Wu[4], Vijay Singh[5], Sinan Wang[1]

[1]Inner Mongolia Water Resource Protection and Utilization Key Laboratory; Water Conservancy and Civil Engineering College, Inner Mongolia Agricultural University, Hohhot 010018, China.

[2]College of Water Sciences, Beijing Normal University, Beijing 100875, China.

[3]State Key Laboratory of Hydroscience and Engineering, Department of Hydraulic Engineering, Tsinghua University, Beijing 100084, China.

[4]Department of Geography, University of Tennessee, Knoxville, TN 37996-0925, USA.

[5]Department of Biological and Agricultural Engineering & Zachry Department of Civil Engineering, Texas A&M University, College Station, TX 77843, USA.

Corresponding author: Tingxi Liu (txliu1966@163.com)

Key Points:

- Ecological and evapotranspiration characteristics of ten typical vegetation communities in semi-arid steppe were refined and decomposed.
- Sensitive parameters of dynamic evapotranspiration improve the regional simulation effect.
- Deep learning was used to downscale regional evapotranspiration at the 3-hour scale.

Abstract

Reports on ecohydrological models for semi-arid steppe basins with scarce historical data are rare. To fully understand the ecohydrological processes in such areas and accurately describe the coupling and mutual feedback between ecological and hydrological processes, a distributed ecohydrological model was constructed, which integrates multi-source information into the MY Ecohydrology (MYEH) model. This paper mainly describes the evapotranspiration module (Eva module) based on sensitive parameters and deep learning. Based on multi-source meteorological, soil, vegetation, and remote sensing data, the historical dynamic characteristics of ten typical vegetation communities in the semi-arid steppe are refined in this study and seven evaporation (ET) components in the Xilin River Basin (XRB) from 1980 to 2018 are simulated. The results show that the Naive Bayesian model constructed based on the temperature and three types of surface reflectance can clearly distinguish between snow-covered or -free conditions. Based on the refinement of typical vegetation communities, the ET process characteristics of different vegetation communities in response to climate change can be determined. Dynamic sensitive parameters significantly improve the regional ET simulation. Based on the validation with the Global Land Evaporation Amsterdam Model product and multiple models in multiple time scales (year, quarter, day, 3 h), a relatively consistent and reliable ET process was obtained for the XRB at the 3-hour scale. The uncertainties of adding and dynamizing more ET process parameters and adjusting the algorithm structure must be further studied.

1 Introduction

An ecohydrological model is a generalized expression of ecohydrological phenomena and processes using mathematical language and physical processes (Svoray et al., 2015), which helps to describe the interaction between ecology and hydrology (Geng et al., 2020) and reveal the succession of ecological patterns and the synergy mechanism of hydrological cycle in ecological processes (Wu et al., 2021a). In recent years, models based on different conservation laws (e.g., water balance, energy balance) and different coupling mechanisms of ecohydrology (one-way transfer or two-way feedback) have been proposed (Grover et al., 2020; Melsen & Guse, 2021) such as the conceptual Hydrologiska Byrans Vattenbalansavdelning (HBV) model (Tong et al., 2021), Xin'anjiang model (Flamig et al., 2020), semi-distributed Topmodel (Beven et al., 2021), distributed Soil and Water Assessment Tool (SWAT) model (Li & Fang, 2021), the distributed hydrological soil vegetation model (DHSVM) (Yan et al., 2021a), Variable Infiltration Capacity (VIC) (Melsen & Guse, 2021), the distributed time variant gain model (DTVGM) (Ma et al., 2019b) and land surface process model Community Land Model (CLM) (Yan et al., 2021b). The results of many studies showed that, based on design and improvement, ecohydrological models exhibit better simulation performances at their respective target scales and ecosystems (Sun et al., 2020a; Yan et al., 2021a).

China's temperate grassland area covers 1.68×10^6 km^2, which accounts for 11.2% of the world total grassland area and is concentrated in the semi-humid and semi-arid areas of the northeastern of China (Wu et al., 2021b). Grassland ecosystems have been degraded due to climate change, excessive grazing, and irrational development (Goenster-Jordan et al., 2021; Yin et al., 2018). Based on ecohydrology, suitable model have been established for ecosystems with abundant water in humid and sub-humid areas (Zha et al., 2020), alpine mountains (Tong et al., 2021), wetlands (Lou et al., 2019), and deserts (Yin et al., 2021). However, ecohydrological models specifically applicable to arid and semi-arid steppe have been rarely reported. The semi-arid grassland ecosystem is relatively barren, although vegetation communities are rich and diverse. The evolution of ecohydrological processes, coupling mechanism, and mutual feedback have strong regional characteristics, which cannot be accurately described with existing models. Therefore, in the context of global ecological governance and protection, it is of great scientific significance to develop and debug an ecohydrological model that is specifically applicable to arid and semi-arid steppe (Ma et al., 2019b).

Evaporation (ET) is important for the water cycle and energy balance as well as for the matter and energy flow between the land and atmosphere (Widmoser & Michel, 2021). The accurate quantification of ET and determination of its spatial and temporal pattern are crucial for understanding the water and energy balance in arid and semi-arid regions in which water is scarce (Varmaghani et al., 2021), physiological characteristics of typical grassland community succession processes, and improving the model accuracy and local water resource management (Dong et al., 2021). Due to the gradual improvement of satellite remote sensing technology, many surface-scale and long-time series ET datasets and models are constantly being introduced (Martens et al., 2017; Miralles et al., 2011; Varmaghani et al., 2021). They can be roughly divided into three categories: ET based on land surface energy balance calculations (Norman et al., 1995), ET based on vegetation index–land surface temperature (LST) triangle/trapezoid model calculations (Long & Singh, 2012), and ET calculated based on Penman–Monteith (P–M) or Priestley–Taylor models (Bao et al., 2020). The above-mentioned methods are also commonly used to calculate the ET in ecohydrological models. For example, Zhang et al. (2021) coupled the VIC model with the crop growth model and introduced an improved ET model based on the soil water stress method to improve the two water stress errors of the Environmental Policy Integrated Climate Model. Bechtold et al. (2019) proposed a set of peatland-specific land surface hydrological modules that significantly improved the performance of peatlands in the global Earth system modeling framework. Based on the situation of different research regions, appropriate ET calculation methods can be selected to improve the requirements with respect to the simulation accuracy of the ecohydrological model (Zhang et al., 2020).

Due to the instantaneity of the remote sensing satellite during data acquisition, there is an uncertainty in the transit gap period between two intervals (Ryu et al., 2012). The model based on the Food and Agriculture Organization (FAO) ET algorithm uses meteorological data-driven and vegetation parameters to calculate the

plant transpiration (E_t), snow evaporation (E_s), soil evaporation (E_b), and canopy interception evaporation (I), which has a high priority in the ET module of the ecohydrological model equal to or longer than the daily time scale (Hu et al., 2015; Long et al., 2014; Vinukollu et al., 2011; Zhang et al., 2008). However, in the semi-arid grassland watershed lacking historical measured data, the use of a single ET algorithm is insufficient to meet the accuracies of both time and space estimations (Hadria et al., 2021; Young et al., 2021). Most ecohydrological models lack surface parameters with high temporal change rates for detailed classification of grassland communities and are also insufficient to distinguish the ET characteristics of multiple vegetation communities in typical grassland in detail (Hulsman et al., 2020; Richards et al., 2020; Sun et al., 2020b). Therefore, in today's widespread application of the Internet of Things and big data, it is of great significance to explore and establish a set of models and methods that include the advantages of various models and data (Yan et al., 2021b) to accurately grasp the ecohydrological process.

The computational model of deep learning is composed of multiple processing layers, and data features on multiple levels of abstraction can be learned through training. After adjusting the model structure and relevant parameters, the model can effectively simulate the real data, thus greatly reducing the workload and time cost, and realizing automatic management of complex transactions (Kratzert et al., 2019). Ecohydrological simulation based on physical and conceptual models requires a grasp of the principles of hydrological processes. However, due to the very complex laws of hydrological phenomena and the difficulty in obtaining many parameters, it is difficult to achieve a good simulation effect (Sit et al., 2020). At this point, the data-driven black box model will show its advantages. By entering long series of data and learning layer by layer inside the model, the eco-hydrological series can be extended well to meet the needs of hydrological work (Shen et al., 2018; Wagener et al., 2010).

Based on the above-mentioned analysis, the MY ecohydrology (MYEH) model was proposed and developed in the study area, that is, the Xilin River Basin (XRB) in the semi-arid steppe, which lacks historical measured data. In this paper, the ET module (in short Eva module) is introduced. The aims of this study were to: (1) establish a downscaling model for the intraday 3-hour snow cover change and determine the compositions of the ET component types; (2) carefully divide typical vegetation communities in the semi-arid steppe and determine corresponding process parameters; 3) analyze dynamic ET-sensitive parameters and optimize ET time series characteristics in the study area; and (4) downscale expanded ET data in combination with multi-source and long-series data and verify existing products and models at multiple scales to ensure the feasibility of the model and expanded data.

2 Materials and Methods

2.1 Study area

The study area is located in the XRB in the Inner Mongolia Autonomous Region, China (43°30”–44°4″ N, 115°37″–117°30″ E), which is characterized by

continental climate in the middle temperate zone. The annual average temperature is 2.6 ℃, the annual ET is significant, and the sunshine is intense (Figure S1). Overall, the terrain is high in the southeast and low in the north, with an elevation ranging from 977 to 1620 m (Figure 1a). In the southeast of the study area, there is a multi-level platform with a high elevation and significant number of gullies. Many fixed dunes are distributed in the middle of the tributary and mainstream. Several of them are semi-fixed dunes with notable wind erosion. More than 90% of the vegetation is natural forage including *Leymus chinensis* Tzvel., *Stipa grandis* P. Smirn., and *Stipa krylovii* Roshev. (Li et al., 2021). A certain amount of *Achnatherum splendens* Nevski can be found in degraded wetlands and surrounding valleys. Many shrubs, such as *Stipa baicalensis* Roshev. and *Caragana microphylla* Lam., can be found in the higher arid steppe. The desert landscape in the central part of the study area is mainly composed of *Ulmus pumila* Linn., whereas *Picea asperata* Mast. and *Betula platyphylla* Suk. are distributed in the northeast (Figure 1b).

According to incomplete statistics, the historical measured data of XRB are relatively scarce. There were only one China's National Hydrological Station (Figure 1b) built in 1964 and one Chinese National Meteorological Station, which was located in the urban area and had little significance to reflect the meteorological conditions of the grassland, in the historical period.

Figure 1. Location, vegetation types (a), and topography (b) of the Xilin River Basin (XRB). SBG: Stipa baicalensis Roshev. grassland; LCG: Leymus chinensis (Trin.) Tzvel. grassland; SKG: Stipa krylovii Roshev. grassland; SGG: Stipa grandis P.A. Smirn. grassland; ASG: Achnatherum splendens (Trin.) Nevski grassland; CMG: Caragana microphylla Lam grassland; AFG: Artemisia frigida Willd. grassland; PAG: Picea asperata Mast. grassland; FSG: Filifolium sibiricum (L.) Kitam. grassland; and WCG: weed community grassland.

2.2 Method

MYEH model is a bidirectional coupling eco-hydrological model for steppe inland river basins in arid and semi-arid regions, which is driven by meteorological data and developed by Dr. Mingyang Li and Prof. Tingxi Liu. In order to get more support from researchers and better improve the model, the model will be released as open source and gradually optimized and updated. The MYEH model mainly includes evapotranspiration, runoff, confluence, grazing disturbance, carbon and nitrogen cycle, etc. It absorbs the advantages of various existing ecological models, hydrological models, as well as the framework and algorithm of eco-hydrological models.

The MYEH-Eva module can be divided into three parts (Figure 2a): judgment, simulation, and validation. The judgment part is used to distinguish the specific types contained in ET. The simulation part is to simulate ET of 3hr scale. The inspection

part is to use the existing products and measured data to test the downscaling ET results.

2.2.1 Eva module judgment part

The judgment part mainly includes three aspects: open waterbody, snow cover, and vegetation–bare soil differentiation. We used historical remote sensing image data (every 5 years) to determine whether a grid contains an open waterbody. If it does, the ET component includes open water surface evaporation (E_w). For the specific waterbody extraction process, area of statistics, and results, please see Zhou et al. (2020). In the area with snow cover, sublimation (E_s) is the main form of ET, whereas ET can be decomposed into bare soil evaporation (E_b), evapotranspiration (E_t) and flow closure loss (I) in areas without snow cover. Especially in the intraday study on the hourly scale, the snow cover may change depending on factors such as the intraday temperature and radiation. It is particularly important to accurately determine whether there the area is covered by snow.

We used temperature, visible light radiation (VIS), near-infrared radiation (NIR), and short-wave radiation (SW) data as input for training the Naive Bayes classifier to judge the snow cover. The detailed model construction and results are provided in Sections 2.3.1 and 4.1. For areas without snow cover, we used Fractional vegetation coverage (FVC) to define E_b or E_t and I, that is, the area with FVC proportion in the grid point is E_t and I and the other area (1-FVC) is E_b. The specific downscaling simulation module is introduced in detail in Section 2.3.2. The actual evapotranspiration (E) in the calculated region of the EVA module of the MYEH model can be decomposed as follows (Figure 2b):

$$E = \begin{cases} E_s, & SC \\ E_t + I + E_b, & Non\ SC, without\ OW, \\ E_t + I + E_b + E_w, & Non\ SC, with\ OW \end{cases} \quad (1)$$

where SC and OW represent snow cover and open water, respectively.

Figure 2. Determination process (a) and decomposition diagram of evaporation (b). VIS: visible radiation; NIR: near-infrared radiation; SW: shortwave radiation; RS: remote sensing; Mete.: meteorological data; Veg.: vegetation data; Alb.: albedo data; FVC: fractional vegetation coverage; E: actual evaporation; E_s: snow sublimation; E_w: open-water evaporation; E_t: transpiration; I: interception loss; and E_b: soil evaporation.

The Naive Bayes classifier is a classification method based on the Bayes theorem and an independent assumption of characteristic conditions (Rahmati et al., 2019). Due to the relatively independent events of snow cover or not, the temperature of the China Meteorological Forcing Dataset (CMFD) and VIS, NIR, and SW of the Global Land Surface Satellite (GLASS) dataset within the scope of the research area

were used as input data and E_s of Global Land Evaporation Amsterdam Model (GLEAM) was used as output for the training judgment.

We established the sample data set $D = \{d_1, d_2, \cdots, d_n\}$. The corresponding characteristic attribute set of the sample data is $X = \{x_1, x_2, \cdots, x_n\}$ and the class variable is $Y = \{y_1, y_2\}$, that is, snow cover and non-snow cover. In this case, D can be divided into two categories, where $x_1, x_2, \cdots, x_n$ are independent of each other and random, Y of the prior data $P_{prior} = P(Y)$, Y of the posterior data $P_{post} = P(Y|X)$, by the Naive Bayes algorithm, a posteriori probability can be made by prior probability $P(Y)$, $P(X)$ of evidence, the type of conditional probability $P(X|Y)$ calculated:

$$P(Y|X) = \frac{P(Y)P(X|Y)}{P(X)} \qquad (2)$$

Because the magnitude of $P(X)$ is fixed, only the molecular part of the above-mentioned equation can be considered during comparisons of posterior probabilities. Therefore, a Naive Bayesian calculation of sample data belonging to category y_i can be carried out as follows:

$$P(y_i|x_1, x_2, \cdots, x_d) = \frac{P(y_i)\prod_{j=1}^{d} P(x_j|y_i)}{\prod_{j=1}^{d} P(x_j)} \qquad (3)$$

2.2.2 Eva module simulation part

The simulation part of the MYEH-Eva module is scaled down by deep learning. In this study, 26 input layers, 7 output layers, and 15 hidden layers were set up for training and the two processes between each layer were the forward propagation of the signal and the backpropagation of the error. This means that the error output is calculated in the direction from input to output, whereas the adjustment weights and thresholds are adjusted in the direction from output to input (Ardabili et al., 2020; Liu et al., 2018b). The number of hidden layers is determined by several simulation tests. Appropriate addition of hidden layers can improve the simulation accuracy and increase the computing load. When the number of hidden layers is greater than or equal to 15, the increase of computing load is much greater than the improvement of simulation accuracy.

A batch gradient descent algorithm was selected as the loss function. Because the objective function to be optimized is very complex, the traditional one-dimensional search method was not used in this study to identify the step size of each iteration. Instead, the update rules of the step size are given to the network in advance to avoid an inefficient algorithm (Hussain et al., 2020; Zhang et al., 2018). The input and output sets of the MYEH-Eva module are shown in Table 2. Based on the description of the Eva module, we first set up a simple model:

$$Y_i^l = f\left(w_{1i}^l x_1^{l-1} + w_{2i}^l x_2^{l-1} + \cdots + w_{ni}^l x_n^{l-1} + b_i^l\right) = \sum_{j=1}^{n} w_{ji}^l x_j^{l-1} +$$

$b_i^l, where\ f(x) = \frac{1}{1+e^{-x}}$, (4)

where the model can be understood as the activation value Y_i^l of neuron $i = 1\ to\ 26$ in layer $l = 1\ to\ 15$, which is equal to each neuron connected to it in the upper layer x_n^{l-1} multiplied by a weight w_{ni}^l. Subsequently, each product is added together, plus a bias quantity b_i^l, and the resulting value is output through a logistic function f in layer l. The parameter Y can be changed into seven ET types. The following concrete models are obtained:

$$Y_i^l = \frac{1}{1+e^{-\left(\sum_{j=1}^{n} w_{ji}^l x_j^{l-1} + b_i^l\right)}} \quad (5)$$

Based on the backpropagation relationship, we set the loss function:

$$J(x) = \frac{1}{2}\sum_{p\in K}\left(O_p - T_p\right)^2, \quad (6)$$

where $K = \{1,2,\cdots,6,7\}$ corresponds to the training results of the seven ET types and O_p and T_p are model outputs and labels of training data, respectively. Our goal was to train the weight values (W) and b at all levels to minimize the loss function $J(x)$. For example, take the partial derivative of the output layer W_{jk}:

$$\frac{\partial J(x)}{W_{jk}} = \frac{\partial \frac{1}{2}\sum_{p\in K}\left(O_p - T_p\right)^2}{\partial W_{jk}} = \frac{1}{2}\sum_{p\in K}(O_k - T_k)\frac{\partial O_k}{\partial W_{jk}} = \frac{1}{2}\sum_{p\in K}(O_k - T_k)\frac{\partial S(x_k)}{\partial W_{jk}} \quad (7)$$

$$= \sum_{p\in K}(O_k - T_k)\,S(x_k)\left(1 - S(x_k)\right)\frac{\partial x_k}{\partial W_{jk}} = \sum_{p\in K}(O_k - T_k)\,O(x_k)\left(1 - O(x_k)\right)\frac{\partial x_k}{\partial W_{jk}}, \quad (8)$$

where $S(x)$ is sigmod function, which is similar to $f(x)$. In the above-mentioned equation, $O_k = S(x_k)$. Therefore, $\frac{\partial S(x_k)}{\partial W_{jk}} = S(x_k)\left(1 - S(x_k)\right)$ and $x_k = O_j W_{jk}$. We then obtain:

$$\frac{\partial x_k}{\partial W_{jk}} = O_j \quad (9)$$

Based on the combination of Eq.(8) and (9), we obtain:

$$\frac{\partial J(x)}{W_{jk}} = \sum_{p\in K}(O_k - T_k)\,O(x_k)\left(1 - O(x_k)\right)O_j \quad (10)$$

If $\delta_k = (O_k - T_k)O(x_k)\left(1 - O(x_k)\right)$, then

$$\frac{\partial J(x)}{W_{jk}} = \sum_{p\in K}\delta_k O_j, \quad (11)$$

where δ_k is residual, that is, the partial derivative of W_{jk}^l corresponding to the k node of the l layer and the j node of the $l-1$ layer is equal to the residual of the layer δ_k^l times the corresponding input value O_j of the j node of the layer above.

Table 2. Input and output variables of the MYEH-Eva module during the training stage.

The 26 input layers of the MYEH-Eva simulation include meteorological, soil, vegetation, and radiation data at the scale of one day. The data can be divided into dynamic and static inputs. Dynamic inputs are time-series variables. Dynamic input in the model corresponds to a set of parameters (English letter in Table 2) and static input is associated with the geographical features of the computing grid, mainly the soil physical and chemical properties of the region. We used eight types of static data corresponding to a set of input parameters (j_1 to j_8) in Table 2. The model training output layer corresponds to 7 ET data at the 1-day scale. In the 3-hour downscaling simulation, we selected 3-hour scale data as input for the model to obtain 3-hour scale ET data. Missing 3-hour scale data were replaced with 1-day scale data of that day. The calculated ET data at the 3-hour scale were combined with the determination of the open waterbody and snow cover and a corresponding zeroing correction was carried out.

2.2.3 EVA module validation part

2.2.3.1 Monthly static parameter simulation

To ensure the accuracy and reliability of the model and its prepared ET data, we used the ET data product, ET employed in the monthly static parameter calculation of the VIC model, and two models utilized for the measured data to carry out a verification at the multi-temporal scale. To describe the growth process of the vegetation according to the general growth regulation of XRB vegetation, we defined April to early June as the beginning of the growing season, mid-June to mid-August as the middle of the growing season, and late August to October as the end of the growing season.

The VIC model is a conceptual distributed hydrological model based on the water and heat balance and a physical dynamic mechanism (Hamman et al., 2018; Lei et al., 2014; Liang et al., 1994; Zhou et al., 2006). To study the effect and sensitivity of dynamic vegetation and albedo parameters on the ET simulation in semi-arid steppe, the monthly static parameters of the VIC model with static vegetation parameters were used as an example in this study to calculate the MYEH-Eva module. The importance of dynamic sensitive parameters for the ecohydrological model was discussed. We decomposed the regional ET method for the VIC model calculation (Eqs 12 to 16). The results show that FVC, leaf area index (LAI), and other variables are important and sensitive parameters of the ET simulation (Fan et al., 2011; Melsen & Guse, 2021). Based on the refinement and dynamization of these parameters, the role of sensitive vegetation parameters in ecohydrological processes and the ET

characteristics of typical vegetation in semi-arid areas under different conditions can be better understood.

$$E = E_p \left\{ \int_0^{A_s} dA + \int_{A_s}^{1} \frac{i_0}{i_m[1-(1-A)^{1/b_i}]} dA \right\} \quad (12)$$

$$E_p = \frac{\Delta R_s + \rho C_b VPD/ra}{\lambda(\Delta + \lambda)} \quad (13)$$

$$E_t = \left[1 - \left(\frac{W_i}{W_{im}}\right)^{2/3}\right] \frac{r_w}{r_w + r_0 + r_c} E_p \quad (14)$$

$$r_c = \frac{r_{0c} g_{sm}}{LAI} \quad (15)$$

$$E_b = \alpha E_p, \quad (16)$$

where A_s is the saturated area; R_s is shortwave radiation; ra is the aerodynamic resistance (s m^{-1}); W_i and W_{im} are the total canopy interception and maximum canopy interception, respectively; r_w and r_0 are the spatial dynamic impedance of water transport and surface evaporation impedance due to the leaf and atmospheric humidity gradient difference, respectively; r_{0c} and g_{sm} are the minimum stomatal impedance of foliage and soil moisture pressure coefficient, respectively; α is the reduction factor; and $(1 - FVC)$ was used to express the area weight for clumped. Definitions of other process parameters can be found in Liang et al. (1994) and Hamman et al. (2018).

2.2.3.2 P–M model

The P–M model is based on the principle of energy balance, principle of water vapor diffusion, and thermal conductivity law of air (Hu et al., 2015; Long et al., 2014). Due to its accuracy and ease of operation, it provides a rigorous and standardized new method for the calculation of the reference crop transpiration (ET_0; (Zhang et al., 2008). The FAO-56 rerecommended the P–M model as the new standard method for calculating ET_0. It has become the mainstream of ET_0 calculations at home and abroad (Hadria et al., 2021; Vinukollu et al., 2011). We put the data measured at weather stations into the P–M model to verify the simulation results at the 1-day and 3-hour scale, respectively. The P–M model can be described as follows (Penman, 1948):

$$ET_0 = \frac{0.408\Delta(R_n - G) + \gamma \frac{900}{T+273} u_2 (e_s - e_a)}{\Delta + \gamma(1 + 0.34u_2)} \quad (17)$$

$$E = (K_{cb} + K_e) \times ET_0, \quad (18)$$

where ET_0 is the reference evapotranspiration (mm day^{-1}); R_n is the net radiation (MJ m^{-2} day^{-1}); G is the soil heat flux density (MJ m^{-2} day^{-1}); T is the mean daily air temperature at 2 m height (°C), u_2 is the wind speed at 2 m height (m s^{-1}); e_s and e_a are the saturation vapor pressure and actual vapor pressure (kPa), respectively;

$e_s - e_a$ represents the saturation vapor pressure deficit (kPa); Δ is the slope vapor pressure curve (kPa °C^{-1}); γ is the psychrometric constant (kPa °C^{-1}); and K_{cb} and K_e are the base crop coefficient and soil moisture evaporation coefficient, respectively.

2.2.3.3 Bowen Ratio-Energy Balance system

The Bowen Ratio-Energy Balance (BREB) method can be used to estimate the latent heat flux to validate the model. The accuracies of the calculated latent and sensible heat fluxes depend on the accuracy of the Bowen ratio (β). The failure of BREB, leading to inconsistent results, has been previously analyzed (Angus & Watts, 1984; Perez et al., 1999). In this study, the selection criteria proposed by Perez et al. (1999) were adopted. The methods are as follows:

$$\lambda ET = \frac{R_n - G}{1 + \beta}, \qquad (19)$$

where λET is the latent heat flux (W m^{-2}), λ is the heat of water vaporization (J kg^{-1}), ET is the evapotranspiration (mm), R_n is the net radiation (W m^{-2}), and G is the ground heat flux (W m^{-2}). The Bowen ratio (β) is defined as follows:

$$\beta = \gamma \frac{\Delta T}{\Delta e}, \qquad (20)$$

where ΔT and Δe are the temperature (°C) and vapor pressure (kPa) difference between the two measurement levels, respectively, and γ is the psychrometric constant (kPa °C^{-1}).

2.3 Evaluation system

The refinement of vegetation communities and optimization of models using sensitive parameters both require a goodness of fit to show the uncertainties and errors of the simulation (Li et al., 2020; Zhang et al., 2019). To more comprehensively evaluate the ET simulation of the MYEH-Eva module in the semi-arid steppe, several evaluation indexes were used in this study. The Taylor diagram (Taylor, 2001) was utilized to plot the modeling situation. Each point represents the vegetation community, type of simulated evapotranspiration, and correlation coefficient and normalized standard deviation of the model. We used the coefficient of determination (R^2), Nash–Sutcliffe efficiency coefficient (NSE; (Nash & Sutcliffe, 1970), model slope, Bias, root-mean-square error (RMSE), mean absolute error (MAE), and Kling-Gupta efficiency (KGE) to quantify the mismatch between the simulation and test data. These parameters can be expressed as:

$$NSE = 1 - \frac{\sum_{n=1}^{N}(O_n - P_n)^2}{\sum_{n=1}^{N}(O_n - \bar{O})^2} \qquad (21)$$

$$Bias = \frac{1}{N}\sum_{n=1}^{N} \bar{P} - E(O) \qquad (22)$$

$$\mathrm{RMSE} = \sqrt{\frac{\sum_{n=1}^{N}(P_n - O_n)^2}{N}} \quad (23)$$

$$MAE = \frac{1}{N}\sum_{n=1}^{N} O_n - P_n \quad (24)$$

$$KGE = \sqrt{(1-\gamma)^2 + (1-\alpha)^2 + (1-\beta)^2} \quad (25)$$

where $\bar{O}$ and $\bar{P}$ are the mean of the observed and predicted data, respectively. The NSE compares the predicted values to the 1:1 line between the measured and predicted values rather than the best regression line through the points. The parameter $E(O)$ represents the expected observed value. γ, α, and β are the linear correlation coefficients, the ratio of their standard deviations and the ratio of their mean values of the simulated and measured values, respectively. In addition, P values were used to test the sample variance of the measured and simulated values and the significance level was set to 0.05. When the p value was less than 0.01, the statistical difference was highly significant.

3 Data

The data used in this paper can be divided into product and measured data, mainly including meteorological, soil, remote sensing satellite, evapotranspiration, vegetation, and reflectivity data. The spatial accuracy and time span of the data are shown in Table 1.

Table 1. Characteristics of the datasets used for the downscaling evapotranspiration comparison.

3.1 Meteorological and soil data

The meteorological data include CMFD and Bowen Ratio meteorological station data obtained in the Shimen Wetland, XRB. The CMFD includes 2 m temperature (T), precipitation (P), relative humidity, 10 m wind speed, short and long wave radiation, and air pressure (Yang et al., 2010). The Bowen Ratio meteorological station is located in the flat wetland before the confluence of the mainstream of the Xilin River and first tributary (Figure 1). I was built in July 2015 and is used to monitor the precipitation, net radiation, air temperature and humidity, wind speed and direction, air pressure, and other meteorological data at heights of 2, 3.5, 5, and 10 m. The collection interval was 5 min and the data collection terminal was a CR1000 data collector (Campbell Scientific Inc., Logan, UT, USA).

The physical and chemical properties of the surface soil in the study area were extracted from the Global Soil Dataset Earth System Modeling (GSDE) dataset (Shangguan & Dai, 2014). The data included the soil particle size, bulk density, soil

moisture characteristics obtained with the negative pressure gauge method, and organic matter content (Shangguan et al., 2014).

3.2 GLEAM

The GLEAM is a set of algorithms that can be used to estimate the ET of different terrestrial components: E, E_t, E_b, I, E_w, E_s, and potential evaporation (E_p). In addition, GLEAM provides the surface and root zone soil moisture and ET stress conditions (Martens et al., 2017). GLEAM calculates the potential evaporation based on the observed net surface radiation and near-surface air temperature. Based on the observed microwave vegetation optical depth (VOD) and estimated root zone soil moisture, the E_p of bare land, high canopy, and short canopy was converted to E by using the multiplier ET stress factor.

3.3 Remote sensing data and GLASS

Landsat TM and OLI images in different historical periods were mainly used for remote sensing satellite data. Because the river course changes were relatively insignificant, one scene was selected for processing every five years during the research period. The GLASS products have been expanded from the original 5 to 14 (Liang et al., 2013a; Liang et al., 2013b). The advantage is that many products have been used for 35 years, that is, from 1981 to the present, which makes it particularly valuable for long-term environmental change research. Radiation products have a spatial resolution of 5 km, which is much finer than common products (such as CERES and GEWEX). All products are continuous in space and time, without gaps or missing values. The wideband longwave emissivity product is the world's first product with an 8-day time resolution and 1 km spatial resolution (Liang et al., 2020).

4 Results

4.1 Determination of snow cover

Based on the snow cover scenario data of more than 4.77 million groups obtained in 39 yr in the study area, Naive Bayes was used to decompose the presence or absence of E_s. The differentiation degree of the four input variables with or without snow cover is shown in Figure 3. A clear snow cover boundary was detected between -10 and 0 ℃ (Friesen et al., 2021; Lin et al., 2021). Three reflectivity indexes use digital number (DN) = 1 as the dividing line; there are overlapping parts on both sides (Usha et al., 2021). The snow cover zone corresponding to the DN value of VIS ranges from 0.15 to 0.6 and 1.25 to 1.5. The bands of the DN values of NIR and SW are close to each other, within the range of 0.25 to 0.5 and 1.35 to 1.5, respectively. Due to the relatively simple ground features in semi-arid steppe, the reflectance of the

three types of steppe has a good regionalization (Chen et al., 2021b; Usha et al., 2021).

Figure 3. Distribution and rug of the temperature (a) and three albedo index parameters (b–d) distinguishing whether the land is covered with snow or not using the Naive Bayesian classifier. In Figure 3a, Ture density = Coordinate axis scale × Scale factor.

4.2 Sensitive parameter analysis

Figure 4 describes the median and 95% confidence interval of the distribution of five sensitive parameters for the dynamic MYEH-Eva module. Two sensitive vegetation parameters (FVC and LAI) were respectively refined in ten typical vegetation communities in the semi-arid steppe and compared with the monthly static parameters based on the VIC model. The results show that there is a large gap between the monthly static values of the two sensitive vegetation parameters and actual historical values obtained from remote sensing (Figures 4a–b). Especially in the middle of the growing season best reflecting the difference between vegetation communities (Anwar, 2021; Tang et al., 2012), the static monthly value of FVC is low, whereas the static monthly value of LAI is high (Lei et al., 2014; Zhai & Tao, 2021). From May to November, the dynamic mean reflectivity is basically consistent with the monthly static values, mainly showing that the dynamic VIS is slightly lower and the other two are slightly higher (Figure 4c). The dispersion degree of the three types of dynamic reflectivity started to increase in November and the dispersion degree increased from December to April. The dynamic mean value is much higher than the monthly static value. Overall, the dynamic mean increases in November and December, peaks in January and February of the following year, and begins to decline in March and April, gradually becoming static on a monthly basis.

Based on the vegetation characteristics of ten typical vegetation communities, three types of common ecohydrological model vegetation types can be classified, that is, open shrub (*Achnatherum splendens* (Trin.) Nevski grassland (ASG) and *Caragana microphylla* Lam grassland (CMG)), closed shrub (*Picea asperata* Mast. grassland (PAG)), and steppe (the other seven vegetation communities). The FVC of the *Stipa baicalensis* Roshev. grassland (SBG) and the four shrub communities growing in the upper reaches of the river basin are always higher than the monthly static values of the grassland types (Figure 4a). The LAI in the study area is low and slowly changes from October to April. In the growing season from May to September, the LAI first increases and then decreases, reaching a peak in July (Tang et al., 2020). The monthly static LAI of the two communities belonging to the open shrub in the growing season is slightly lower than the dynamic average, whereas the values of the other vegetation communities are higher than the dynamic average (Figure 4b).

Figure 4. Distributions of the FVC (a), LAI (b), and albedo (c) data to which the evaporation module of the VIC model was most sensitive for the different individual biomes. The boxes represent the 95% confidence interval and the vertical line represents the median. Gray points and dash-dotted lines represent the original values of the five parameters in the VIC model. LAI: leaf area index. VIC model: Variable Infiltration Capacity model.

4.3 Parameter calibration of Eva module

We input the 1-day scale data shown in Table 2 into Eq. (5) to calculate the weight parameters of the model. Based on the snow cover, open water, and FVC, the existence of ET was determined and the simulation results of the training period were output. Figure 5 compares the performance of six evapotranspiration types in the training period for ten typical vegetation communities. The two axes represent the normalized standard deviation (σ) of the simulated values and the curve represents Pearson's correlation coefficient. Table 3 shows the average weight parameters of each hidden layer of the Eva module.

Figure 5. Taylor diagram comparing the MYEH-Eva module performance in the training stage for six types of evaporation for ten individual biomes. MYEH-Eva module: MY ecohydrology model evaporation module.

Table 3. Weight values of the hidden, input, and output layers in the actual evaporation simulation of the MYEH-Eva module of semi-arid grassland.

The results show that the performance of the algorithm varies with different ET types. For different ET types, the model's correlation coefficient of the simulation of E, E_t, E_b, and E_w is close to 1, whereas the correlation coefficient of E_s is slightly lower, ranging from 0.7–0.8. The differences in the vegetation communities are also reflected in the model simulations. On one hand, the simulated value σ of ET varies according to different vegetation communities and σ of SBG is the highest overall, whereas that of *Stipa krylovii* Roshev. grassland (SKG) is the lowest. On the other hand, the vegetation community also affects the simulation accuracy of E and ET (Figure 5a).

4.4 Scale expansion and validation

By substituting the prepared 3-hour scale input data, seven types of 3-hour scale ET data were obtained for the XRB from 1980 to 2018. The evaluation results of the downscaling model using various evaluation indexes are shown in Table 4. We

used Eq. (1) to calculate the E value of the study area. To verify the accuracy of the data simulation and availability of the model, the GLEAM products and P–M and BREB models were used in this study, respectively, to substitute the measured data and the data were tested at two scales (1-day and 3-hour).

The 1-day scale modeling evaluation results show that the overall quality of the Eva module with respect to the simulation of ET in the XRB is good, with a high model reliability, R^2 and NSE between 0.57–0.98, and the lowest ASG accuracy along the river (Table 4). The results show that the simulation performance of E, E_p, E_s, and E_t was better for the ten typical vegetation types in the study area, with R^2 and NSE higher than 0.85 and 0.65, respectively, whereas E_b and I of some vegetation types are slightly lower than the average. In particular, the NSE of E_b and I under SBG, LCG, AFG, and PAG ranges from 0.42–0.56 (Figures 6a and c). In terms of errors, the absolute errors of E, E_p, and E_t are slightly higher than those of the other three evapotranspiration types, ranging from 0.2–0.4 mm. However, the overall error dispersion of the model is small. All errors are below 0.1 mm, that is, the RMSE is at a relatively low level (Figures 6b and d). Regardless of the classification of typical vegetation, in the surface scale E simulation test, the simulation in the area near 43°34 "N is poor, which is mainly represented by the low R^2 and NSE (Figures 6e and f) and slightly higher MAE (Figure 6h) of these grid points. The RMSE of the whole region remains at a good level (Figure 6g).

Table 4. Summary statistics for the performance of the MYEH-Eva module in the training and simulation stages for ten individual biomes in semi-arid grassland.

Figure 6. Results of the evaporation simulation with the MYEH-Eva module. (a–b) Accuracy and error of the evaporation simulation for ten individual biomes. (c–d) Mean precision and error of the simulation results for different evapotranspiration types. (e–h) Simulation results for the actual evaporation in the XRB. Statistical indicators: R^2 and Rsq: regression goodness of fit; NSE: Nash–Sutcliffe efficiency coefficient; RMSE: root-mean-square error; MAE: mean absolute error.

The downscaling results of the ET and Eva modules were simulated by using the ET product data GLEAM and the two ET models (P-M and BREB model) brought in the measured meteorological data, respectively. The results show that the downscaled ET data maintain a high correlation with GLEAM (Figures 7a and b), with an R^2 value of 0.83. The E calculated by the FAO P–M and BREB models is overall consistent with the value obtained from the Eva module simulation, but there is a certain degree of overestimation in the spring and summer (Figures 7c and d). As expected, the peak value of E calculated by using the monthly static parameters of the

VIC model is observed nearly one month earlier (Figure 7a) and the interannual characteristics of the ET in the basin are lost.

Figure 7. Comparison of the daily actual evaporation obtained with the MYEH-Eva module and four types of validation data from 1980 to 2018 in the XRB. The actual daily evaporation of the MYEH-Eva and BREB models were converted from 3-hour data. (a–b) Comparison between the values obtained from the Eva, VIC model, and GLEAM; (c–d) Comparison between the Eva module result and values obtained with the FAO Penman–Monteith (P–M) and BREB models. GLEAM: Global Land Evaporation Amsterdam Model; BREB: Bowen Ratio-Energy balance method.

The intraday simulated E obtained with the Eva and FAO P–M models insignificantly differ. The intraday trend of the latent heat flux (λET) calculated with the BREB model from January to August is basically consistent with that of the EVA and FAO P–M models. In the case of constant coordinate size, the intraday variation in the λET from September to December is significantly higher than that of the above-mentioned two models (Figure 8a). The results of the correlation analysis show that the R^2 of the Eva and FAO P–M models are both higher than 0.7 from January to April and from May to August, but slightly lower from September to December (Figure 8b). The R^2 of the BREB model λET after the Eva module and unit conversion is higher than 0.8 from January to April and from September to December and the fitting performance is poor from May to August (Figure 8c).

Figure 8. Comparison of the 3-hourly evapotranspiration simulated using three models, that is, the MYEH-Eva, P–M, and BREB models. The actual evaporation (E) in (a) was calculated with the MYEH-Eva and P–M models. The latent heat flux (λET) was calculated using the BREB model. Validation data used in this figure includes the period from October 2015 to October 2016.

5 Discussion

5.1 The discriminant system of ET type

The Naive Bayesian model performs well with respect to the determination of snow cover in semi-arid steppe (Cordeiro et al., 2021) and the four indicators selected in this study exhibit a good degree of differentiation. The maximum temperature with snow cover in the study area is 12–15 ℃ (Figure 3a), which generally occurs during sunny winter days, whereas the minimum temperature without snow cover is -30 ℃ (Figure 3a). At this time, the temperature is no longer a decisive factor. The reality is that there is no snow in the area (Lin et al., 2021). This also shows that the importance of snow cover can be determined by combining the multi-index system of the surface

reflectance (Usha et al., 2021). It is difficult to describe the complex and changeable hydrological process in detail with a single index (Chen et al., 2021b; Fu et al., 2021).

Compared with the air temperature, the DN values of the three surface reflectance indexes are relatively concentrated and approximate to the normal distribution (Figures 3b–d), which is also the consistency characteristic of the surface reflectance of snow cover in different regions (Chen et al., 2021b; Fu et al., 2021; Usha et al., 2021). In the absence of snow cover, the distribution of NIR in the range of its DN value less than 0.5 is more uniform than that of VIS and SW (Figure 3b), which also indicates that NIR yields a better resolution in the mixed pixels of vegetation, soil, and snow (Liu et al., 2013). Qu et al. (2016) showed that the surface reflectance of the GLASS dataset better reflects the snow particle size. In our snow cover decision module, the DN values of the three types of surface reflectance all show subwave peaks between 0.5–0.7 and 1.15–1.3. The results of previous studies suggested that this is due to surface ice–water mixing during snow melt (Feng et al., 2016; Qu et al., 2014).

5.2 Dynamic sensitive parameters

Ecohydrological models that use monthly static parameters to simulate the ET have a considerable uncertainty over time (Anwar, 2021; Lei et al., 2014; Liu et al., 2018a; Zhai & Tao, 2021). To simulate ET datasets that are more consistent with regional characteristics, researchers have established optimal parameters representing the heterogeneity of the land surface and vegetation (Anwar, 2021; Bennett et al., 2018; Jimenez-Gutierrez et al., 2019). Due to the low degree of vegetation refinement in most current ecohydrological models (Hulsman et al., 2020; Richards et al., 2020; Sun et al., 2020b), it is of great significance to identify and understand the key parameters in the ET algorithm of the ecohydrological model and analyze their interactions for further optimization (Lei et al., 2014; Liu et al., 2018a). The comparison of the ET results calculated by monthly static parameters and dynamic sensitive parameters shows that the interannual distribution of E calculated by static parameters is significantly advanced (Figure 7a), which is directly related to the inconsistent peak time of vegetation sensitive parameters observed in the results in the middle of the growing season (Figures 4a–b).

The FVC is a sensitive parameter that can be used to determine the ET type (Dash et al., 2021; Tesemma et al., 2015). It directly determines the composition ratio of E_b, E_t, and I (Fan et al., 2011). The results of parameter sensitivity analysis showed that the FVC of typical vegetation communities in semi-arid steppe is 5% at the beginning and end of the growing season and on average 15%–30% in the middle of the growing season (Li et al., 2021), which is higher than the monthly static value (Figure 4a). The average LAI (Eq. 9) in the growing season, which directly affects the resistance coefficient of the vegetation canopy in the ET simulation, is only between 0.8–2, that is, much lower than the monthly static index (Figure 4b). The notable difference between the two planting parameters of typical vegetation communities is

due to the unique vegetation characteristics of semi-arid steppe (Hu et al., 2021), which are mainly related to the physiological and ecological characteristics of typical vegetation in semi-arid steppe with small leaves and many clusters (Tang et al., 2020). To adapt to the dry and water-deficient environment, plants have to reduce their leaf area to reduce the water loss (Hu et al., 2021; Niu et al., 2016; Qin et al., 2014). For example, Caragana microphylla, a typical plant of CMG, grows in Horqin Sandy Land, a semi-arid area with slightly humid climate. The LAI in the growing season of Caragana microphylla in this area is 2 to 4 times that observed in the XRB (Bao et al., 2021).

In addition to the numerical differences every month, the annual characteristics of the two sensitive vegetation parameters also differ (Zhou et al., 2006). In the XRB, the spring temperature rises slowly and the vegetation FVC and LAI have a low growth range from April to June, whereas the peak value lags one month behind (Figures 4a and b;(Guo et al., 2019). This is clearly reflected in the ET simulation, that is, the E simulated with monthly static parameters is observed approximately one month earlier than other model waveforms (Figures 7a and c). Another advantage of using dynamically sensitive parameters is that they can more accurately simulate the ecohydrological response process in the context of climate change (Shiklomanov et al., 2021; Zhang et al., 2019). For example, in the three wet seasons of 1992–1994, 1998–1999, and 2012–2013, the vegetation growth status in the XRB was significantly better than that of the static parameters, resulting in the simulation of a significantly lower E based on static parameters.

In the simulation of regional ecohydrological processes, the refinement of typical vegetation communities is beneficial for a more accurate description of the ET and seasonal characteristics of different vegetation communities (Dzikiti et al., 2014; Everwand et al., 2014; Ma et al., 2019a). The spatial heterogeneity of nature can be better expressed. In the modeling process, the simulated σ value of ET and the simulation accuracy of E and E_t change with the vegetation community (Figure 5). On one hand, the ET law of a vegetation day and growing season differs and the ET dispersion degree significantly differs. This is also the reason why only E and E_t, which are closely related to the vegetation characteristics, show heterogeneous simulation accuracies (Dzikiti et al., 2014; Rubert et al., 2018). On the other hand, the ET simulation results of FSG and WCG show a certain degree of difference, that is, the simulation accuracy of one part is slightly lower than that of the other part (Figure 5a), which is due to the performance of the same vegetation community in different geographical locations and ecological environments (Carmona et al., 2016). The results of previous studies showed that grids with a slightly lower simulation accuracy in WCG are located closer to rivers and the ecohydrological interaction becomes more complex in wet environments, leading to a slight decrease in the correlation (Ahmad et al., 2020; Hwang et al., 2020).

The XRB glaciation period lasts for five months. In the study area, the actual surface reflectance from December to April of the next year is 2 to 4 times of the calibrated value due to the effects of snow and ice coverage (Figure 4c). To simplify

the operation of most ecohydrological models, only the reflectance of vegetation is used as a parameter (Lei et al., 2014; Tesemma et al., 2015; Zhai & Tao, 2021). Such a generalization will cause huge errors in simulations in cold and arid regions (Di Stefano et al., 2019; Samadi et al., 2020). Furthermore, in areas with a low FVC, the vegetation reflectance is used to replace the actual surface reflectance, which is not representative in complex mixed pixels (Lyu et al., 2020). In general, the sensitive parameters of the vegetation community and dynamic ET simulation are refined and the ecological characteristics and environmental realities of vegetation community are considered (Nietupski et al., 2021). It is helpful to clarify the coupling mechanism and threshold system of the ecohydrological process in the grassland watershed and to reshape the historical evolution of the ecohydrological process (Gregory et al., 2019; Jautzy et al., 2021) to quantitatively assess the response and mutual feedbacks between ecohydrological processes in grassland catchments under climate change.

5.3 Intraday ET expansion analysis

During the test of the intraday ET expansion, multiple indicator tests objectively described the performance of the downscaling simulation of the Eva module in which the R^2 of E, E_b, E_p, and E_t was higher while the NSE was slightly decreased (Figure 6a). The NSE is very sensitive to extreme values and a small number of outliers in the simulation results leads to a decline in the NSE (Moriasi et al., 2007; Nash & Sutcliffe, 1970). Daily ET values of semi-arid steppe tend to be small. For example, E, E_p, and E_t differ by an order of magnitude from ET components of other types. Therefore, the MAE of the three parameters will be relatively high (Figure 6d), but this does not mean that the model has a large error (Baik et al., 2018). To improve the accuracy of the simulation, the Eva module uses data scaling during training and simulation. The order of magnitude of the input dataset is enlarged before training the data and the order of magnitude is reduced according to the original proportion after simulating the output dataset.

In the surface scale E simulation test, a relatively notable simulation misjudgment zone appeared in the middle of the XRB and several grid points of this misjudgment zone showed a low NSE (Figure 6f) and high MAE (Figure 6h) for the same vegetation type. This is similar to the results obtained by Satge et al. (2019) who used a GLEAM dataset to test the ET in the arid Andean Plateau. They suggested that the GLEAM dataset may be more suitable for spatial ET tests. It does not conform to local ET dynamics at a small number of lattice points (Baik et al., 2018; Huang et al., 2019; Satge et al., 2019).

The use of a GLEAM dataset yielded a high degree of consistency in the test of EVA module (Figures 7a and b), indicating that the Eva module has a good ET simulation capability. Compared with the GLEAM model driven by remote sensing data, the MYEH-Eva module driven by meteorological, soil, vegetation, and remote sensing data also has a stronger adaptability to climate change. In the summer of 1998–1999 with excessive precipitation, E simulated by the Eva module significantly

improved compared with that in adjacent years (Figure 7a). Generally speaking, the P–M model, as a single leaf model, does not consider E_b and I. In spring and autumn with less vegetation, E_t should be lower than that obtained with the MYEH model considering E_b and I (Bao et al., 2021; Bao et al., 2020; Hadria et al., 2021; Lin et al., 2021). However, our actual test results in the XRB differ (Figure 7c), which is due to the slight discrepancy between the measured meteorological data used in the P–M model and the CMFD. The BREB test results have a good control of the ET peak value (Perez et al., 1999). The above-mentioned analysis also shows that the precipitation is the main factor affecting the multi-year ET peak transformation in the semi-arid steppe basin (Acharya & Sharma, 2021; Yang et al., 2021).

5.4 Uncertainty analysis

Although the MYEH-Eva module yields a high fit in the ET downscaling simulation in the XRB, there is room for further improvement. The continuous transport process of water in the soil–plant–atmosphere continuum should be considered and the height of vegetation and resistance coefficient of the typical vegetation canopy should be added to the model to describe ET (Chen et al., 2021a; Lee et al., 2021; Nyolei et al., 2021). Even after optimization, the EVA module still has shortcomings. The Eva module should be optimized with respect to two aspects: underfitting and overfitting.

To address underfitting problems, training can be continued by increasing the number of iterations, changing algorithms, increasing the number of parameters and complexity of the model, or using Boosting and other integration methods (Bennett & Nijssen, 2021; Vulova et al., 2021). To address the overfitting problem, we can indirectly reduce the number of neuron layers and use different Sigmoid functions (Eqs 7 and 8) to fit from different aspect and learn from each other. In addition, ET with different types of components also causes a significant uncertainty. The Eva module parameters can be further optimized by adding field flux data and other available observation data (e.g., eddy correlation, LAS, lysimeter) to improve the simulation accuracy.

6 Conclusion

Based on multi-source meteorological, soil, vegetation, and surface reflectance data, we subdivided ten typical vegetation communities in semi-arid steppe in this study, constructed a MYEH-Eva module, and established a discrimination system composed of ET components using Naive Bayes, FVC, and remote sensing images. The performances of dynamic sensitive parameters and monthly static parameters in ten typical vegetation communities were compared. The downscale simulation of seven ET components at the regional 3-hour scale was carried out and multiple spatiotemporal scales were used to verify the results obtained from various models. The results show that the dynamic sensitive parameters reflect the ecological

characteristics of different typical vegetation communities and truly describe the evolution of the regional ET under climate change. The E of the downscaling simulation has passed the test of various models at the annual, seasonal, daily, and 3-hour scales, respectively, and has a good accuracy and availability, which is beneficial for the application of the MYEH model in the simulation of ecohydrological processes in semi-arid steppe. The module has several shortcomings with respect to the parameter configuration and internal model and thus must be further optimized and adjusted to improve the simulation accuracy.

Acknowledgement: This research was funded by the National Natural Science Foundation of China (Nos. 51939006 and 51620105003), the Inner Mongolia Major science and technology projects (Nos. 2020ZD0009 and 2019ZD007), the Inner Mongolia Science and Technology Plan Project (Nos. 2020 and 2021GG0071), the Ministry of Education Innovative Research Team (No. IRT_17R60), the Innovation Team in Priority Areas Accredited by the Ministry of Science and Technology (No. 2015RA4013), the Inner Mongolia Industrial Innovative Research Team (No. 2012), the Natural Science Foundation of Inner Mongolia Autonomous Region of China (Nos. 2020JQ06 and 2019BS05001), the Research and Innovation Funding Project for Graduate Students (BZ2020069). We are grateful to the principal investigators and their teams of all the dataset used in this study. The CMFD datasets are available at http://data.tpdc.ac.cn/en/data/8028b944-daaa-4511-8769-965612652c49/. GLEAM datasets are available at https://www.gleam.eu/. GSDE datasets are available at http://www.tpdc.ac.cn/zh-hans/data/2e46eb77-3ca2-4b90-9a42-fd49f10630d4/. GLASS datasets are available at http://www.glass.umd.edu/Download.html. All generated methods used in this study can be downloaded from https://github.com/myli1993/MYEH_Downscaling-expansion-of-evaporation-based-on-refinement-of-sensitive-parameters. And generated data can be downloaded from https://pan.baidu.com/s/1b64StoFNrZVMKPIFAz_VhA and the extract code is MYEH. The authors declare no conflict of interest.

Author Contributions: M.L. developed the initial and final versions of this manuscript and analyzed the data. T.L., L.M., L.D., Y.W., G.W., H.L., Q.W., and V.S. contributed their expertise and insights, overseeing the analysis. S.W. helped perform part of the calculation.

References

Acharya, B., & Sharma, V. (2021). Comparison of Satellite Driven Surface Energy Balance Models in Estimating Crop Evapotranspiration in Semi-Arid to Arid Inter-Mountain Region. *Remote Sensing, 13*(9), 31. doi: 10.3390/rs13091822

Ahmad, S., Hormann, G., Zantout, N., & Schrautzer, J. (2020). Quantifying actual evapotranspiration in fen ecosystems: Implications of management and vegetation structure. *Ecohydrology & Hydrobiology, 20*(3), 382-396. doi: 10.1016/j.ecohyd.2020.04.001

Angus, D. E., & Watts, P. J. (1984). Evapotranspiration — How good is the Bowen ratio method? *Agricultural Water Management, 8*(1), 133-150. doi: 10.1016/0378-3774(84)90050-7

Anwar, S. A. (2021). On the contribution of dynamic leaf area index in simulating the African climate using a regional climate model (RegCM4). *Theoretical and Applied Climatology, 143*(1-2), 119-129. doi: 10.1007/s00704-020-03414-x

Ardabili, S., Mosavi, A., Dehghani, M., & Várkonyi-Kóczy, A. R. (2020). *Deep Learning and Machine Learning in Hydrological Processes Climate Change and Earth Systems a Systematic Review*, Cham.

Baik, J., Liaqat, U. W., & Choi, M. (2018). Assessment of satellite- and reanalysis-based evapotranspiration products with two blending approaches over the complex landscapes and climates of Australia. *Agricultural and Forest Meteorology, 263*, 388-398. doi: 10.1016/j.agrformet.2018.09.007

Bao, Y. Z., Duan, L. M., Liu, T. X., Tong, X., Wang, G. Q., Lei, H. M., et al. (2021). Simulation of evapotranspiration and its components for the mobile dune using an improved dual-source model in semi-arid regions. *Journal of Hydrology, 592*, 11. doi: 10.1016/j.jhydrol.2020.125796

Bao, Y. Z., Duan, L. M., Tong, X., Liu, T. X., Wang, G. L., Zhang, L., & Singh, V. P. (2020). Simulation and partition evapotranspiration for the representative landform-soil-vegetation formations in Horqin Sandy Land, China. *Theoretical and Applied Climatology, 140*(3-4), 1221-1232. doi: 10.1007/s00704-020-03165-9

Bechtold, M., De Lannoy, G. J. M., Koster, R. D., Reichle, R. H., Mahanama, S. P., Bleuten, W., et al. (2019). PEAT-CLSM: A Specific Treatment of Peatland Hydrology in the NASA Catchment Land Surface Model. *Journal of Advances in Modeling Earth Systems, 11*(7), 2130-2162. doi: 10.1029/2018ms001574

Bennett, A., & Nijssen, B. (2021). Deep Learned Process Parameterizations Provide Better Representations of Turbulent Heat Fluxes in Hydrologic Models. *Water Resources Research, 57*(5). doi: 10.1029/2020wr029328

Bennett, K. E., Blanco, J. R. U., Jonko, A., Bohn, T. J., Atchley, A. L., Urban, N. M., & Middleton, R. S. (2018). Global Sensitivity of Simulated Water Balance Indicators Under Future Climate Change in the Colorado Basin. *Water Resources Research, 54*(1), 132-149. doi: 10.1002/2017wr020471

Beven, K. J., Kirkby, M. J., Freer, J. E., & Lamb, R. (2021). A history of TOPMODEL. *Hydrology and Earth System Sciences, 25*(2), 527-549. doi: 10.5194/hess-25-527-2021

Carmona, A. M., Poveda, G., Sivapalan, M., Vallejo-Bernal, S. M., & Bustamante, E. (2016). A scaling approach to Budyko's framework and the complementary relationship of evapotranspiration in humid environments: case study of the Amazon River basin. *Hydrology and Earth System Sciences, 20*(2), 589-603. doi: 10.5194/hess-20-589-2016

Chen, H., Huang, J. J., McBean, E., & Singh, V. P. (2021a). Evaluation of alternative two-source remote sensing models in partitioning of land evapotranspiration. *Journal of Hydrology, 597*. doi: 10.1016/j.jhydrol.2021.126029

Chen, X., Yang, Y., Ma, Y., & Li, H. (2021b). Distribution and Attribution of Terrestrial Snow Cover Phenology Changes over the Northern Hemisphere during 2001-2020. *Remote Sensing, 13*(9). doi: 10.3390/rs13091843

Cordeiro, M. C. R., Martinez, J. M., & Pena-Luque, S. (2021). Automatic water detection from multidimensional hierarchical clustering for Sentinel-2 images and a comparison with Level 2A processors. *Remote Sensing of Environment, 253*, 17. doi: 10.1016/j.rse.2020.112209

Dash, S. S., Sahoo, B., & Raghuwanshi, N. S. (2021). How reliable are the evapotranspiration estimates by Soil and Water Assessment Tool (SWAT) and Variable Infiltration Capacity (VIC) models for

catchment-scale drought assessment and irrigation planning? *Journal of Hydrology, 592*, 22. doi: 10.1016/j.jhydrol.2020.125838

Di Stefano, C., Nicosia, A., Palmeri, V., Pampalone, V., & Ferro, V. (2019). Comparing flow resistance law for fixed and mobile bed rills. *Hydrological Processes, 33*(26), 3330-3348. doi: 10.1002/hyp.13561

Dong, G., Zhao, F., Chen, J., Qu, L., Jiang, S., Chen, J., & Shao, C. (2021). Divergent forcing of water use efficiency from aridity in two meadows of the Mongolian Plateau. *Journal of Hydrology, 593*. doi: 10.1016/j.jhydrol.2020.125799

Dzikiti, S., Jovanovic, N. Z., Bugan, R., Israel, S., & Le Maitre, D. C. (2014). Measurement and modelling of evapotranspiration in three fynbos vegetation types. *Water Sa, 40*(2), 189-198. doi: 10.4314/wsa.v40i2.1

Everwand, G., Fry, E. L., Eggers, T., & Manning, P. (2014). Seasonal Variation in the Capacity for Plant Trait Measures to Predict Grassland Carbon and Water Fluxes. *Ecosystems, 17*(6), 1095-1108. doi: 10.1007/s10021-014-9779-z

Fan, Y., van den Dool, H. M., & Wu, W. R. (2011). Verification and Intercomparison of Multimodel Simulated Land Surface Hydrological Datasets over the United States. *Journal of Hydrometeorology, 12*(4), 531-555. doi: 10.1175/2011jhm1317.1

Feng, Y. B., Liu, Q., Qu, Y., & Liang, S. L. (2016). Estimation of the Ocean Water Albedo From Remote Sensing and Meteorological Reanalysis Data. *IEEE TRANSACTIONS ON GEOSCIENCE AND REMOTE SENSING, 54*(2), 850-868. doi: 10.1109/tgrs.2015.2468054

Flamig, Z. L., Vergara, H., & Gourley, J. J. (2020). The Ensemble Framework For Flash Flood Forecasting (EF5) v1.2: description and case study. *Geoscientific Model Development, 13*(10), 4943-4958. doi: 10.5194/gmd-13-4943-2020

Friesen, H. C., Slesak, R. A., Karwan, D. L., & Kolka, R. K. (2021). Effects of snow and climate on soil temperature and frost development in forested peatlands in minnesota, USA. *Geoderma, 394*, 12. doi: 10.1016/j.geoderma.2021.115015

Fu, D. L., Zhang, W., Xing, Y. F., Li, H. Z., Wang, P. J., Li, B., et al. (2021). Impacts of maximum snow albedo and land cover changes on meteorological variables during winter in northeast China. *Atmospheric Research, 254*, 15. doi: 10.1016/j.atmosres.2021.105449

Geng, X. J., Zhou, X. C., Yin, G. D., Hao, F. H., Zhang, X., Hao, Z. C., et al. (2020). Extended growing season reduced river runoff in Luanhe River basin. *Journal of Hydrology, 582*, 9. doi: 10.1016/j.jhydrol.2019.124538

Goenster-Jordan, S., Ingold, M., Jannoura, R., Buerkert, A., & Joergensen, R. G. (2021). Soil microbial properties of subalpine steppe soils at different grazing intensities in the Chinese Altai Mountains. *Scientific Reports, 11*(1), 8. doi: 10.1038/s41598-021-81120-y

Gregory, S., Wildman, R., Hulse, D., Ashkenas, L., & Boyer, K. (2019). Historical changes in hydrology, geomorphology, and floodplain vegetation of the Willamette River, Oregon. *River Research and Applications, 35*(8), 1279-1290. doi: 10.1002/rra.3495

Grover, S., Tayal, S., Beldring, S., & Li, H. (2020). Modeling Hydrological Processes in Ungauged Snow-Fed Catchment of Western Himalaya. *Water Resources, 47*(6), 987-995. doi: 10.1134/s0097807820060147

Guo, J., Yang, X., Niu, J., Jin, Y., Xu, B., Shen, G., et al. (2019). Remote sensing monitoring of green-up dates in the Xilingol grasslands of northern China and their correlations with meteorological factors. *International Journal of Remote Sensing, 40*(5-6), 2190-2211. doi:

10.1080/01431161.2018.1506185

Hadria, R., Benabdelouhab, T., Lionboui, H., & Salhi, A. (2021). Comparative assessment of different reference evapotranspiration models towards a fit calibration for arid and semi-arid areas. *Journal of Arid Environments, 184*, 10. doi: 10.1016/j.jaridenv.2020.104318

Hamman, J. J., Nijssen, B., Bohn, T. J., Gergel, D. R., & Mao, Y. (2018). The Variable Infiltration Capacity model version 5 (VIC-5): infrastructure improvements for new applications and reproducibility. *Geoscientific Model Development, 11*, 3481-3496. doi: 10.5194/gmd-11-3481-2018

Hu, G. C., Jia, L., & Menenti, M. (2015). Comparison of MOD16 and LSA-SAF MSG evapotranspiration products over Europe for 2011. *Remote Sensing of Environment, 156*, 510-526. doi: 10.1016/j.rse.2014.10.017

Hu, H. Y., Zhu, L., Li, H. X., Xu, D. M., & Xie, Y. Z. (2021). Seasonal changes in the water-use strategies of three herbaceous species in a native desert steppe of Ningxia, China. *Journal of Arid Land, 13*(2), 109-122. doi: 10.1007/s40333-021-0051-z

Huang, S. C., Eisner, S., Magnusson, J. O., Lussana, C., Yang, X., & Beldring, S. (2019). Improvements of the spatially distributed hydrological modelling using the HBV model at 1 km resolution for Norway. *Journal of Hydrology, 577*, 19. doi: 10.1016/j.jhydrol.2019.03.051

Hulsman, P., Winsemius, H. C., Michailovsky, C. I., Savenije, H. H. G., & Hrachowitz, M. (2020). Using altimetry observations combined with GRACE to select parameter sets of a hydrological model in a data-scarce region. *Hydrology and Earth System Sciences, 24*(6), 3331-3359. doi: 10.5194/hess-24-3331-2020

Hussain, D., Hussain, T., Khan, A. A., Naqvi, S. A. A., & Jamil, A. (2020). A deep learning approach for hydrological time-series prediction: A case study of Gilgit river basin. *Earth Science Informatics, 13*(3), 915-927. doi: 10.1007/s12145-020-00477-2

Hwang, K., Chandler, D. G., & Shaw, S. B. (2020). Patch scale evapotranspiration of wetland plant species by ground-based infrared thermometry. *Agricultural and Forest Meteorology, 287*, 13. doi: 10.1016/j.agrformet.2020.107948

Jautzy, T., Maltais, M., & Buffin-Belanger, T. (2021). Interannual evolution of hydrosedimentary connectivity induced by forest cover change in a snow-dominated mountainous catchment. *Land Degradation & Development, 32*(7), 2318-2335. doi: 10.1002/ldr.3902

Jimenez-Gutierrez, J. M., Valero, F., Jerez, S., & Montavez, J. P. (2019). Impacts of Green Vegetation Fraction Derivation Methods on Regional Climate Simulations. *Atmosphere, 10*(5), 17. doi: 10.3390/atmos10050281

Kratzert, F., Herrnegger, M., Klotz, D., Hochreiter, S., & Klambauer, G. (2019). NeuralHydrology – Interpreting LSTMs in Hydrology. In W. Samek, G. Montavon, A. Vedaldi, L. K. Hansen, & K.-R. Müller (Eds.), *Explainable AI: Interpreting, Explaining and Visualizing Deep Learning* (pp. 347-362). Cham: Springer International Publishing.

Lee, S.-J., Kim, N., & Lee, Y. (2021). Development of Integrated Crop Drought Index by Combining Rainfall, Land Surface Temperature, Evapotranspiration, Soil Moisture, and Vegetation Index for Agricultural Drought Monitoring. *Remote Sensing, 13*(9). doi: 10.3390/rs13091778

Lei, H. M., Huang, M. Y., Leung, L. R., Yang, D. W., Shi, X. Y., Mao, J. F., et al. (2014). Sensitivity of global terrestrial gross primary production to hydrologic states simulated by the Community Land Model using two runoff parameterizations. *Journal of Advances in Modeling Earth Systems, 6*(3), 658-679. doi: 10.1002/2013ms000252

Li, C. Y., & Fang, H. Y. (2021). Assessment of climate change impacts on the streamflow for the Mun River

in the Mekong Basin, Southeast Asia: Using SWAT model. *Catena, 201*, 13. doi: 10.1016/j.catena.2021.105199

Li, M., Liu, T., Duan, L., Luo, Y., Ma, L., Wang, Y., et al. (2020). Scale transfer and simulation of the infiltration in chestnut soil in a semi-arid grassland basin. *Ecological Engineering, 158*, 106045. doi: 10.1016/j.ecoleng.2020.106045

Li, M., Liu, T., Luo, Y., Duan, L., Ma, L., Wang, Y., et al. (2021). Fractional vegetation coverage downscaling inversion method based on Land Remote-Sensing Satellite (System, Landsat-8) and polarization decomposition of Radarsat-2. *International Journal of Remote Sensing, 42*(9), 3255-3276. doi: 10.1080/01431161.2020.1871093

Liang, S., Cheng, C., Jia, K., Jiang, B., Liu, Q., Xiao, Z., et al. (2020). The Global LAnd Surface Satellite (GLASS) products suite. *Bulletin of the American Meteorological Society*. doi: 10.1175/BAMS-D-18-0341.1

Liang, S., Zhang, X., Xiao, Z., Cheng, J., Liu, Q., & Zhao, X. (2013a). Global LAnd Surface Satellite (GLASS) products: Algorithms, validation and analysis. *Springer*. doi:

Liang, S. L., Zhao, X., Liu, S. H., Yuan, W. P., Cheng, X., Xiao, Z. Q., et al. (2013b). A long-term Global LAnd Surface Satellite (GLASS) data-set for environmental studies. *International Journal of Digital Earth, 6*, 5-33. doi: 10.1080/17538947.2013.805262

Liang, X., Lettenmaier, D. P., Wood, E. F., & Burges, S. J. (1994). A simple hydrologically based model of land surface water and energy fluxes for general circulation models. *Journal of Geophysical Research: Atmospheres, 99*(D7), 14415-14428. doi: 10.1029/94JD00483

Lin, Y. W., Cai, T. J., Ju, C. Y., & Cui, X. Q. (2021). Applicability evaluation and improvement of different snow evaporation calculation methods in the Great Xing'an mountains. *Earth Science Informatics*, 12. doi: 10.1007/s12145-021-00597-3

Liu, M. L., Adam, J. C., Richey, A. S., Zhu, Z. C., & Myneni, R. B. (2018a). Factors controlling changes in evapotranspiration, runoff, and soil moisture over the conterminous US: Accounting for vegetation dynamics. *Journal of Hydrology, 565*, 123-137. doi: 10.1016/j.jhydrol.2018.07.068

Liu, N. F., Liu, Q., Wang, L. Z., Liang, S. L., Wen, J. G., Qu, Y., & Liu, S. H. (2013). A statistics-based temporal filter algorithm to map spatiotemporally continuous shortwave albedo from MODIS data. *Hydrology and Earth System Sciences, 17*(6), 2121-2129. doi: 10.5194/hess-17-2121-2013

Liu, T., Abd-Elrahman, A., Morton, J., & Wilhelm, V. L. (2018b). Comparing fully convolutional networks, random forest, support vector machine, and patch-based deep convolutional neural networks for object-based wetland mapping using images from small unmanned aircraft system. *Giscience & Remote Sensing, 55*(2), 243-264. doi: 10.1080/15481603.2018.1426091

Long, D., Longuevergne, L., & Scanlon, B. R. (2014). Uncertainty in evapotranspiration from land surface modeling, remote sensing, and GRACE satellites. *Water Resources Research, 50*(2), 1131-1151. doi: 10.1002/2013wr014581

Long, D., & Singh, V. P. (2012). A Two-source Trapezoid Model for Evapotranspiration (TTME) from satellite imagery. *Remote Sensing of Environment, 121*, 370-388. doi: 10.1016/j.rse.2012.02.015

Lou, H. Z., Yang, S. T., Hao, F. H., Jiang, L. M., Zhao, C. S., Ren, X. Y., et al. (2019). SMAP, RS-DTVGM, and in-situ monitoring: Which performs best in presenting the soil moisture in the middle-high latitude frozen area in the Sanjiang Plain, China? *Journal of Hydrology, 571*, 300-310. doi: 10.1016/j.jhydrol.2018.12.023

Lyu, X., Li, X. B., Dang, D. L., Dou, H. S., Xuan, X. J., Liu, S. Y., et al. (2020). A new method for grassland

degradation monitoring by vegetation species composition using hyperspectral remote sensing. *Ecological Indicators, 114*, 10. doi: 10.1016/j.ecolind.2020.106310

Ma, F., Luo, L. F., Ye, A. Z., & Duan, Q. Y. (2019a). Drought Characteristics and Propagation in the Semiarid Heihe River Basin in Northwestern China. *Journal of Hydrometeorology, 20*(1), 59-77. doi: 10.1175/jhm-d-18-0129.1

Ma, F., Ye, A. Z., & Duan, Q. Y. (2019b). Seasonal drought ensemble predictions based on multiple climate models in the upper Han River Basin, China. *Climate Dynamics, 53*(12), 7447-7460. doi: 10.1007/s00382-017-3577-1

Martens, B., Miralles, D. G., Lievens, H., van der Schalie, R., de Jeu, R. A. M., Fernandez-Prieto, D., et al. (2017). GLEAM v3: satellite-based land evaporation and root-zone soil moisture. *Geoscientific Model Development, 10*(5), 1903-1925. doi: 10.5194/gmd-10-1903-2017

Melsen, L. A., & Guse, B. (2021). Climate change impacts model parameter sensitivity - implications for calibration strategy and model diagnostic evaluation. *Hydrology and Earth System Sciences, 25*(3), 1307-1332. doi: 10.5194/hess-25-1307-2021

Miralles, D. G., Holmes, T. R. H., De Jeu, R. A. M., Gash, J. H., Meesters, A., & Dolman, A. J. (2011). Global land-surface evaporation estimated from satellite-based observations. *Hydrology and Earth System Sciences, 15*(2), 453-469. doi: 10.5194/hess-15-453-2011

Moriasi, D. N., Arnold, J. G., Van Liew, M. W., Bingner, R. L., Harmel, R. D., & Veith, T. L. (2007). Model evaluation guidelines for systematic quantification of accuracy in watershed simulations. *Transactions of the ASABE, 50*(3), 885-900. doi: 10.13031/2013.23153

Nash, J. E., & Sutcliffe, J. E. (1970). River flow forecasting through conceptual models. Part 1 - A discussion of principles. *Journal of Hydrology, 10*, 282-290. doi: 10.1016/0022-1694(70)90255-6

Nietupski, T. C., Kennedy, R. E., Temesgen, H., & Kerns, B. K. (2021). Spatiotemporal image fusion in Google Earth Engine for annual estimates of land surface phenology in a heterogenous landscape. *International Journal of Applied Earth Observation and Geoinformation, 99*, 15. doi: 10.1016/j.jag.2021.102323

Niu, F. R., Duan, D. P., Chen, J., Xiong, P. F., Zhang, H., Wang, Z., & Xu, B. C. (2016). Eco-Physiological Responses of Dominant Species to Watering in a Natural Grassland Community on the Semi-Arid Loess Plateau of China. *Frontiers in Plant Science, 7*, 11. doi: 10.3389/fpls.2016.00663

Norman, J. M., Kustas, W. P., & Humes, K. S. (1995). Source approach for estimating soil and vegetation energy fluxes in observations of directional radiometric surface temperature. *Agricultural and Forest Meteorology, 77*(3), 263-293. doi: 10.1016/0168-1923(95)02265-Y

Nyolei, D., Diels, J., Mbilinyi, B., Mbungu, W., & van Griensven, A. (2021). Evapotranspiration simulation from a sparsely vegetated agricultural field in a semi-arid agro-ecosystem using Penman-Monteith models. *Agricultural and Forest Meteorology, 303*, 22. doi: 10.1016/j.agrformet.2021.108370

Penman, H. L. (1948). Natural Evaporation from Open Water, Bare Soil and Grass. *Proceedings of the Royal Society of London. Series A, Mathematical and Physical Sciences, 193*(1032), 120-145. doi:

Perez, P. J., Castellvi, F., Ibañez, M., & Rosell, J. I. (1999). Assessment of reliability of Bowen ratio method for partitioning fluxes. *Agricultural and Forest Meteorology, 97*(3), 141-150. doi: 10.1016/S0168-1923(99)00080-5

Qin, Y., Yi, S., Ren, S., Li, N., & Chen, J. (2014). Responses of typical grasslands in a semi-arid basin on the

Qinghai-Tibetan Plateau to climate change and disturbances. *Environmental Earth Sciences, 71*(3), 1421-1431. doi: 10.1007/s12665-013-2547-0

Qu, Y., Liang, S., Liu, Q., Li, X., Feng, Y., & Liu, S. (2016). Estimating Arctic sea-ice shortwave albedo from MODIS data. *Remote Sensing of Environment, 186*, 32-46. doi: 10.1016/j.rse.2016.08.015

Qu, Y., Liu, Q., Liang, S. L., Wang, L. Z., Liu, N. F., & Liu, S. H. (2014). Direct-Estimation Algorithm for Mapping Daily Land-Surface Broadband Albedo From MODIS Data. *IEEE TRANSACTIONS ON GEOSCIENCE AND REMOTE SENSING, 52*(2), 907-919. doi: 10.1109/tgrs.2013.2245670

Rahmati, O., Ghorbanzadeh, O., Teimurian, T., Mohammadi, F., Tiefenbacher, J. P., Falah, F., et al. (2019). Spatial Modeling of Snow Avalanche Using Machine Learning Models and Geo-Environmental Factors: Comparison of Effectiveness in Two Mountain Regions. *Remote Sensing, 11*(24), 26. doi: 10.3390/rs11242995

Richards, D. R., Moggridge, H. L., Warren, P. H., & Maltby, L. (2020). Impacts of hydrological restoration on lowland river floodplain plant communities. *Wetlands Ecology and Management, 28*(3), 403-417. doi: 10.1007/s11273-020-09717-0

Rubert, G. C., Roberti, D. R., Pereira, L. S., Quadros, F. L. F., Velho, H. F. D., & de Moraes, O. L. L. (2018). Evapotranspiration of the Brazilian Pampa Biome: Seasonality and Influential Factors. *Water, 10*(12), 18. doi: 10.3390/w10121864

Ryu, Y., Baldocchi, D. D., Black, T. A., Detto, M., Law, B. E., Leuning, R., et al. (2012). On the temporal upscaling of evapotranspiration from instantaneous remote sensing measurements to 8-day mean daily-sums. *Agricultural and Forest Meteorology, 152*, 212-222. doi: 10.1016/j.agrformet.2011.09.010

Samadi, S., Pourreza-Bilondi, M., Wilson, C., & Hitchcock, D. B. (2020). Bayesian Model Averaging With Fixed and Flexible Priors: Theory, Concepts, and Calibration Experiments for Rainfall-Runoff Modeling. *Journal of Advances in Modeling Earth Systems, 12*(7), 28. doi: 10.1029/2019ms001924

Satge, F., Hussain, Y., Xavier, A., Zola, R. P., Salles, L., Timouk, F., et al. (2019). Unraveling the impacts of droughts and agricultural intensification on the Altiplano water resources. *Agricultural and Forest Meteorology, 279*, 13. doi: 10.1016/j.agrformet.2019.107710

Shangguan, W., & Dai, Y. (2014). The global soil dataset for earth system modeling. *A Big Earth Data Platform for Three Poles*. doi: 10.11888/Soil.tpdc.270578

Shangguan, W., Dai, Y. J., Duan, Q. Y., Liu, B. Y., & Yuan, H. (2014). A global soil data set for earth system modeling. *Journal of Advances in Modeling Earth Systems, 6*(1), 249-263. doi: 10.1002/2013ms000293

Shen, C., Laloy, E., Elshorbagy, A., Albert, A., Bales, J., Chang, F.-J., et al. (2018). HESS Opinions: Incubating deep-learning-powered hydrologic science advances as a community. *Hydrology and Earth System Sciences, 22*(11), 5639-5656. doi: 10.5194/hess-22-5639-2018

Shiklomanov, A. N., Dietze, M. C., Fer, I., Viskari, T., & Serbin, S. P. (2021). Cutting out the middleman: calibrating and validating a dynamic vegetation model (ED2-PROSPECT5) using remotely sensed surface reflectance. *Geoscientific Model Development, 14*(5), 2603-2633. doi: 10.5194/gmd-14-2603-2021

Sit, M., Demiray, B. Z., Xiang, Z., Ewing, G. J., Sermet, Y., & Demir, I. (2020). A comprehensive review of deep learning applications in hydrology and water resources. *Water Science and Technology, 82*(12), 2635-2670. doi: 10.2166/wst.2020.369

Sun, R. C., Hernandez, F., Liang, X., & Yuan, H. L. (2020a). A Calibration Framework for High-Resolution

Hydrological Models Using a Multiresolution and Heterogeneous Strategy. *Water Resources Research, 56*(8), 26. doi: 10.1029/2019wr026541

Sun, Y., Hou, F. J., Angerer, J. P., & Yi, S. H. (2020b). Effects of topography and land-use patterns on the spatial heterogeneity of terracette landscapes in the Loess Plateau, China. *Ecological Indicators, 109*, 9. doi: 10.1016/j.ecolind.2019.105839

Svoray, T., Assouline, S., & Katul, G. (2015). Introduction to a special section on ecohydrology of semiarid environments: Confronting mathematical models with ecosystem complexity. *Water Resources Research, 51*(11), 8677-8683. doi: 10.1002/2015wr018131

Tang, L., He, M.-Z., Xu, H., & Jia, P.-C. (2020). Validation of vegetation coverage and NDVI based on UAV remote sensing method and its response to hydrothermal gradient (In Chinese). *The journal of applied ecology, 31*(1), 35-44. doi: 10.13287/j.1001-9332.202001.014

Tang, Q. H., Vivoni, E. R., Munoz-Arriola, F., & Lettenmaier, D. P. (2012). Predictability of Evapotranspiration Patterns Using Remotely Sensed Vegetation Dynamics during the North American Monsoon. *Journal of Hydrometeorology, 13*(1), 103-121. doi: 10.1175/jhm-d-11-032.1

Taylor, K. E. (2001). Summarizing multiple aspects of model performance in a single diagram. *Journal of Geophysical Research: Atmospheres, 106*(D7), 7183-7192. doi: 10.1029/2000JD900719

Tesemma, Z. K., Wei, Y., Peel, M. C., & Western, A. W. (2015). Including the dynamic relationship between climatic variables and leaf area index in a hydrological model to improve streamflow prediction under a changing climate. *Hydrology and Earth System Sciences, 19*(6), 2821-2836. doi: 10.5194/hess-19-2821-2015

Tong, R., Parajka, J., Salentinig, A., Pfeil, I., Komma, J., Szeles, B., et al. (2021). The value of ASCAT soil moisture and MODIS snow cover data for calibrating a conceptual hydrologic model. *Hydrology and Earth System Sciences, 25*(3), 1389-1410. doi: 10.5194/hess-25-1389-2021

Usha, K. H., Nair, V. S., & Babu, S. S. (2021). Effect of aerosol-induced snow darkening on the direct radiative effect of aerosols over the Himalayan region. *Environmental Research Letters, 16*(6), 9. doi: 10.1088/1748-9326/abf190

Varmaghani, A., Eichinger, W. E., & Prueger, J. H. (2021). A meteorological-based crop coefficient model for estimation of daily evapotranspiration. *Hydrological Processes, 35*(2), 16. doi: 10.1002/hyp.14025

Vinukollu, R. K., Wood, E. F., Ferguson, C. R., & Fisher, J. B. (2011). Global estimates of evapotranspiration for climate studies using multi-sensor remote sensing data: Evaluation of three process-based approaches. *Remote Sensing of Environment, 115*(3), 801-823. doi: 10.1016/j.rse.2010.11.006

Vulova, S., Meier, F., Rocha, A. D., Quanz, J., Nouri, H., & Kleinschmit, B. (2021). Modeling urban evapotranspiration using remote sensing, flux footprints, and artificial intelligence. *The Science of the total environment, 786*, 147293. doi: 10.1016/j.scitotenv.2021.147293

Wagener, T., Sivapalan, M., Troch, P. A., McGlynn, B. L., Harman, C. J., Gupta, H. V., et al. (2010). The future of hydrology: An evolving science for a changing world. *Water Resources Research, 46*(5). doi: https://doi.org/10.1029/2009WR008906

Widmoser, P., & Michel, D. (2021). Partial energy balance closure of eddy covariance evaporation measurements using concurrent lysimeter observations over grassland. *Hydrology and Earth System Sciences, 25*(3), 1151-1163. doi: 10.5194/hess-25-1151-2021

Wu, Y. Y., Huang, L., Zhao, C. W., Chen, M. H., & Ouyang, W. (2021a). Integrating hydrological, landscape ecological, and economic assessment during hydropower exploitation in the upper Yangtze

River. *Science of the Total Environment, 767*, 12. doi: 10.1016/j.scitotenv.2021.145496

Wu, Z. J., Zhang, J. H., Deng, F., Zhang, S., Zhang, D., Xun, L., et al. (2021b). Fusion of GF and MODIS Data for Regional-Scale Grassland Community Classification with EVI2 Time-Series and Phenological Features. *Remote Sensing, 13*(5), 19. doi: 10.3390/rs13050835

Yan, H. X., Sun, N., Fullerton, A., & Baerwalde, M. (2021a). Greater vulnerability of snowmelt-fed river thermal regimes to a warming climate. *Environmental Research Letters, 16*(5), 13. doi: 10.1088/1748-9326/abf393

Yan, Y., Tang, J., Wang, S., Niu, X., & Wang, L. (2021b). Uncertainty of land surface model and land use data on WRF model simulations over China. *Climate Dynamics*. doi: 10.1007/s00382-021-05778-w

Yang, J. H., Wang, W., Hua, T. T., & Peng, M. (2021). Spatiotemporal variation of actual evapotranspiration and its response to changes of major meteorological factors over China using multi-source data. *Journal of Water and Climate Change, 12*(2), 325-338. doi: 10.2166/wcc.2020.221

Yang, K., He, J., Tang, W. J., Qin, J., & Cheng, C. C. K. (2010). On downward shortwave and longwave radiations over high altitude regions: Observation and modeling in the Tibetan Plateau. *Agricultural and Forest Meteorology, 150*(1), 38-46. doi: 10.1016/j.agrformet.2009.08.004

Yin, S. Q., Zhu, Z. Y., Wang, L., Liu, B. Y., Xie, Y., Wang, G. N., & Li, Y. S. (2018). Regional soil erosion assessment based on a sample survey and geostatistics. *Hydrology and Earth System Sciences, 22*(3), 1695-1712. doi: 10.5194/hess-22-1695-2018

Yin, X. W., Feng, Q., Zheng, X. J., Zhu, M., Wu, X., Guo, Y., et al. (2021). Spatio-temporal dynamics and eco-hydrological controls of water and salt migration within and among different land uses in an oasis-desert system. *Science of the Total Environment, 772*, 12. doi: 10.1016/j.scitotenv.2021.145572

Young, D. J. N., Jeronimo, S. M. A., Churchill, D. J., Kane, V. R., & Latimer, A. M. (2021). The utility of climatic water balance for ecological inference depends on vegetation physiology assumptions. *Global Ecology and Biogeography, 30*(5), 933-949. doi: 10.1111/geb.13277

Zha, X. N., Xiong, L. H., Guo, S. L., Kim, J. S., & Liu, D. D. (2020). AR-GARCH with Exogenous Variables as a Postprocessing Model for Improving Streamflow Forecasts. *Journal of Hydrologic Engineering, 25*(8), 16. doi: 10.1061/(asce)he.1943-5584.0001955

Zhai, R., & Tao, F. L. (2021). Climate Change in China Affects Runoff and Terrestrial Ecosystem Water Retention More Than Changes in Leaf Area Index and Land Use/Cover Over the Period 1982-2015. *Journal of Geophysical Research-Biogeosciences, 126*(4), 19. doi: 10.1029/2020jg005902

Zhang, K., Zhu, G., Ma, J., Yang, Y., Shang, S., & Gu, C. (2019). Parameter Analysis and Estimates for the MODIS Evapotranspiration Algorithm and Multiscale Verification. *Water Resources Research, 55*(3), 2211-2231. doi: 10.1029/2018WR023485

Zhang, L., Ren, D., Nan, Z. T., Wang, W. Z., Zhao, Y., Zhao, Y. B., et al. (2020). Interpolated or satellite-based precipitation? Implications for hydrological modeling in a meso-scale mountainous watershed on the Qinghai-Tibet Plateau. *Journal of Hydrology, 583*, 15. doi: 10.1016/j.jhydrol.2020.124629

Zhang, L., Wang, F., Sun, T., & Xu, B. (2018). A constrained optimization method based on BP neural network. *Neural Computing & Applications, 29*(2), 413-421. doi: 10.1007/s00521-016-2455-9

Zhang, Y. L., Wu, Z. Y., Singh, V. P., He, H., He, J., Yin, H., & Zhang, Y. X. (2021). Coupled hydrology-crop growth model incorporating an improved evapotranspiration module. *Agricultural Water*

Management, 246, 19. doi: 10.1016/j.agwat.2020.106691

Zhang, Y. Q., Chiew, F. H. S., Zhang, L., Leuning, R., & Cleugh, H. A. (2008). Estimating catchment evaporation and runoff using MODIS leaf area index and the Penman-Monteith equation. *Water Resources Research, 44*(10), 15. doi: 10.1029/2007wr006563

Zhou, S. Q., Chen, J. M., Peng, G., & Xue, G. Y. (2006). Effects of heterogeneous vegetation on the surface hydrological cycle. *Advances in Atmospheric Sciences, 23*(3), 391-404. doi: 10.1007/s00376-006-0391-9

Zhou, Y., Liu, T., Duan, L., Wang, Y., Li, X., & Li, M. (2020). Driving force analysis and landscape pattern evolution in the up stream valley of Xilin River Basin (In Chinese). *Arid Zone Research, 37*(3), 580-590. doi: 10.13866/j.azr.2020.03.05

Figures

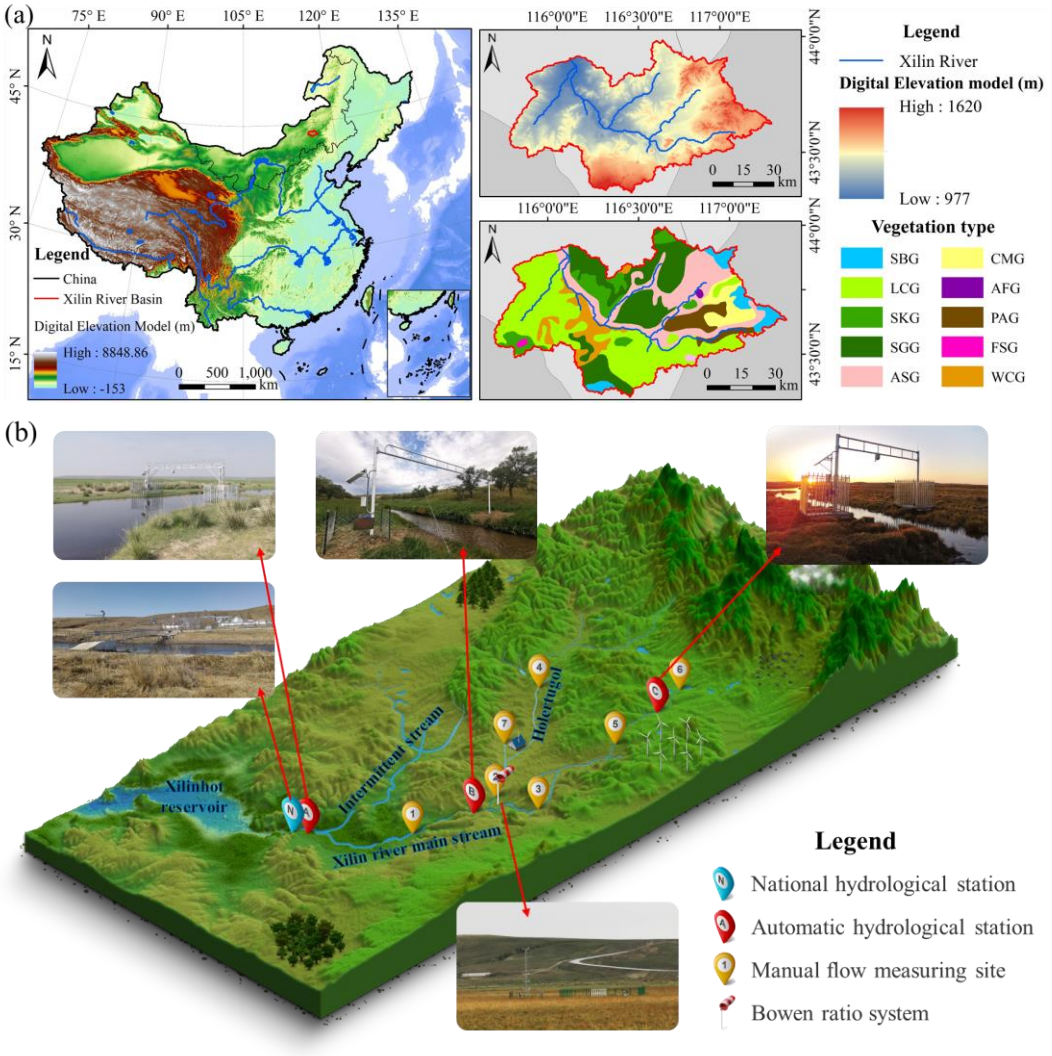

Figure 1. Location, vegetation types (a), and topography (b) of the Xilin River Basin (XRB). SBG: Stipa baicalensis Roshev. grassland; LCG: Leymus chinensis (Trin.) Tzvel. grassland; SKG: Stipa krylovii Roshev. grassland; SGG: Stipa grandis P.A. Smirn. grassland; ASG: Achnatherum splendens (Trin.) Nevski grassland; CMG: Caragana microphylla Lam grassland; AFG: Artemisia frigida Willd. grassland; PAG: Picea asperata Mast. grassland; FSG: Filifolium sibiricum (L.) Kitam. grassland; and WCG: weed community grassland.

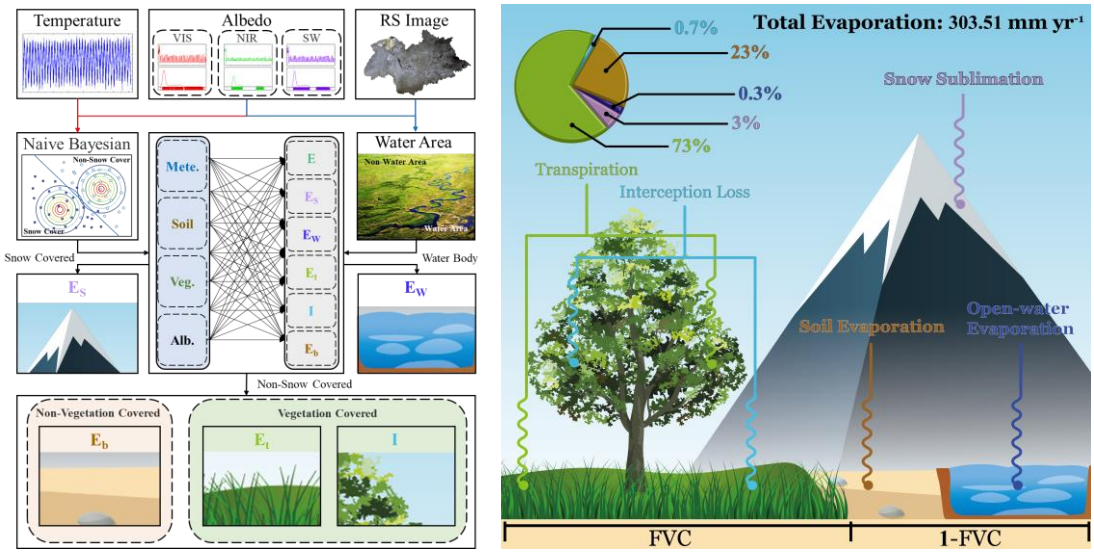

Figure 2. Determination process (a) and decomposition diagram of evaporation (b). VIS: visible radiation; NIR: near-infrared radiation; SW: shortwave radiation; RS: remote sensing; Mete.: meteorological data; Veg.: vegetation data; Alb.: albedo data; FVC: fractional vegetation coverage; E: actual evaporation; E_S: snow sublimation; E_W: open-water evaporation; E_t: transpiration; I: interception loss; and E_b: soil evaporation.

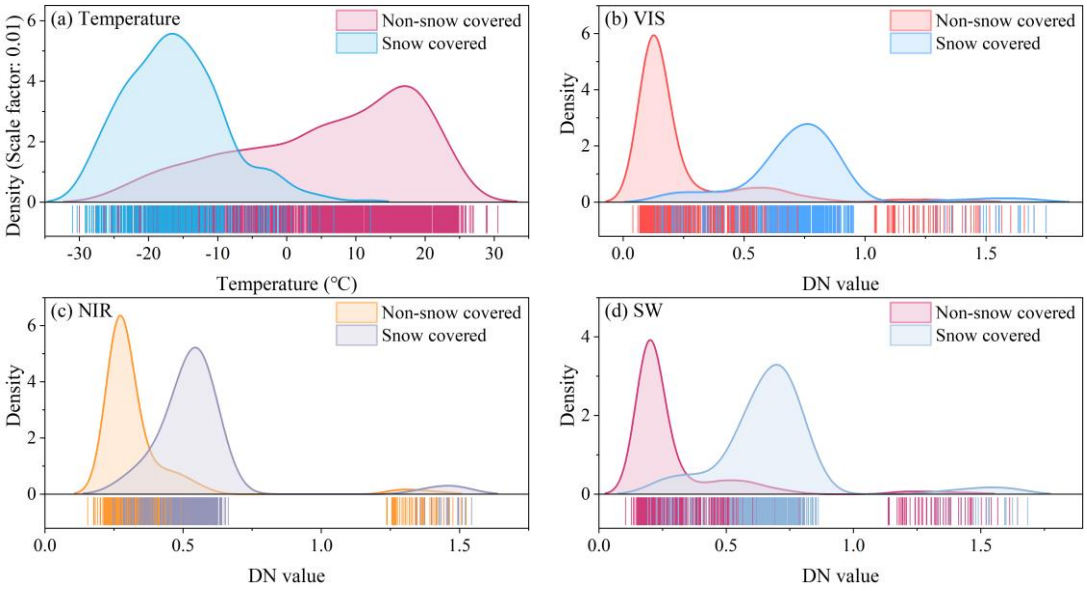

Figure 3. Distribution and rug of the temperature (a) and three albedo index parameters (b–d) distinguishing whether the land is covered with snow or not using the Naive Bayesian classifier. In Figure 3a, Ture density = Coordinate axis scale × Scale factor.

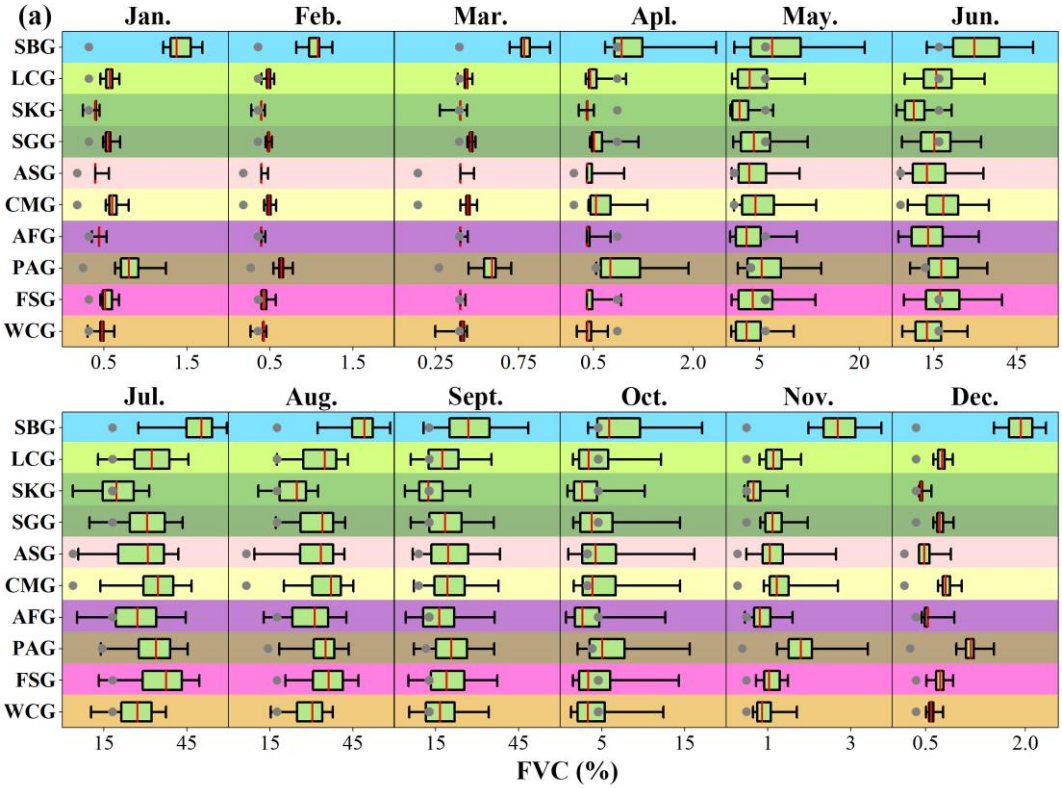
(a)
Jan.
Feb.
Mar.
Apl.
May.
Jun.
SBG
LCG
SKG
SGG
ASG
CMG
AFG
PAG
FSG
WCG
0.5 1.5 0.5 1.5 0.25 0.75 0.5 2.0 5 20 15 45
Jul.
Aug.
Sept.
Oct.
Nov.
Dec.
15 45 15 45 15 45 5 15 1 3 0.5 2.0
FVC (%)

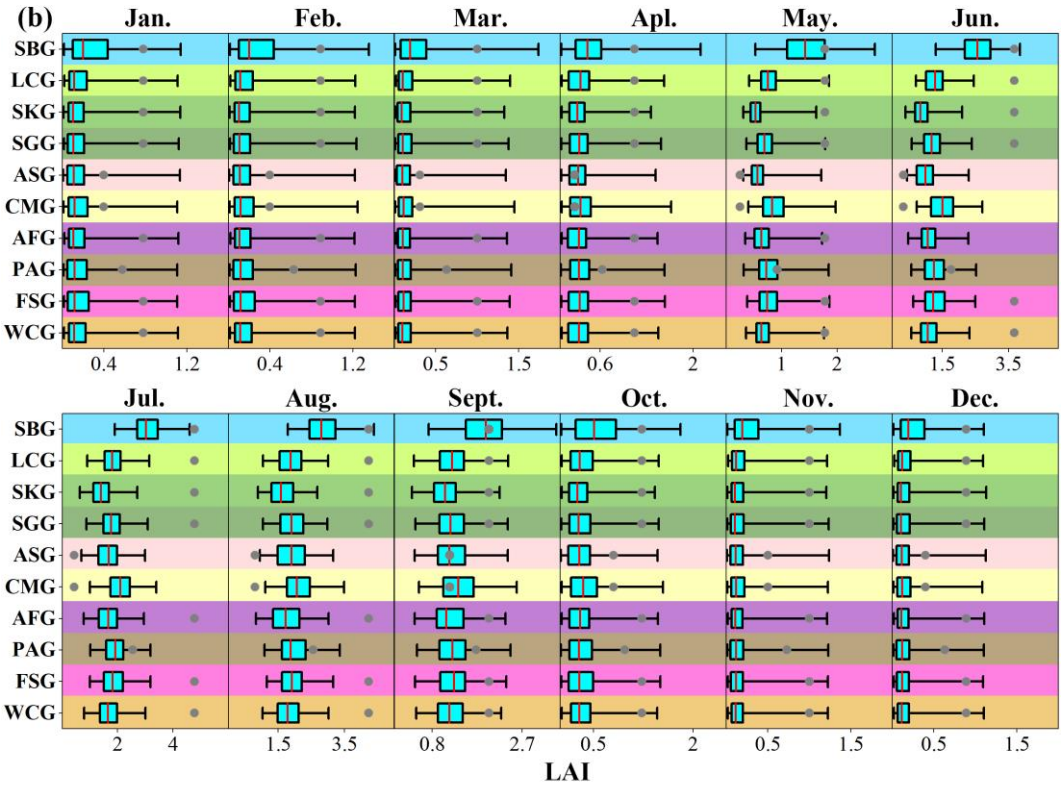
(b)
Jan.
Feb.
Mar.
Apl.
May.
Jun.
SBG
LCG
SKG
SGG
ASG
CMG
AFG
PAG
FSG
WCG
0.4 1.2 0.4 1.2 0.5 1.5 0.6 2 1 2 1.5 3.5
Jul.
Aug.
Sept.
Oct.
Nov.
Dec.
2 4 1.5 3.5 0.8 2.7 0.5 2 0.5 1.5 0.5 1.5
LAI

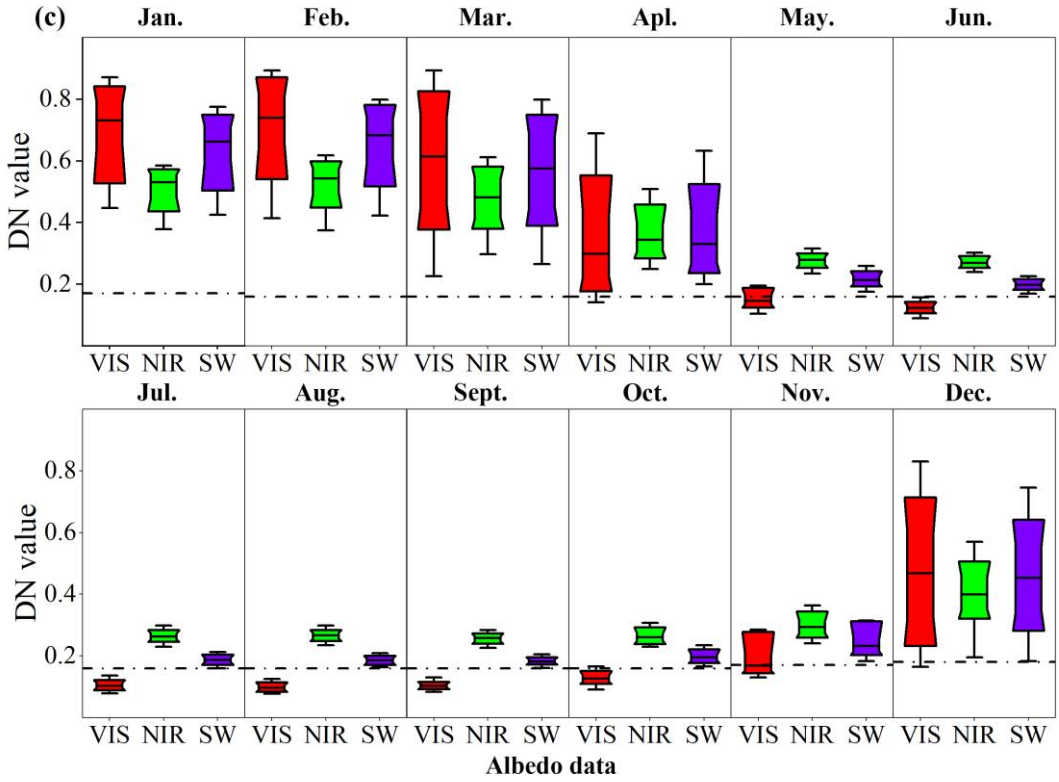

Figure 4. Distributions of the FVC (a), LAI (b), and albedo (c) data to which the evaporation module of the VIC model was most sensitive for the different individual biomes. The boxes represent the 95% confidence interval and the vertical line represents the median. Gray points and dash-dotted lines represent the original values of the five parameters in the VIC model. LAI: leaf area index. VIC model: Variable Infiltration Capacity model.

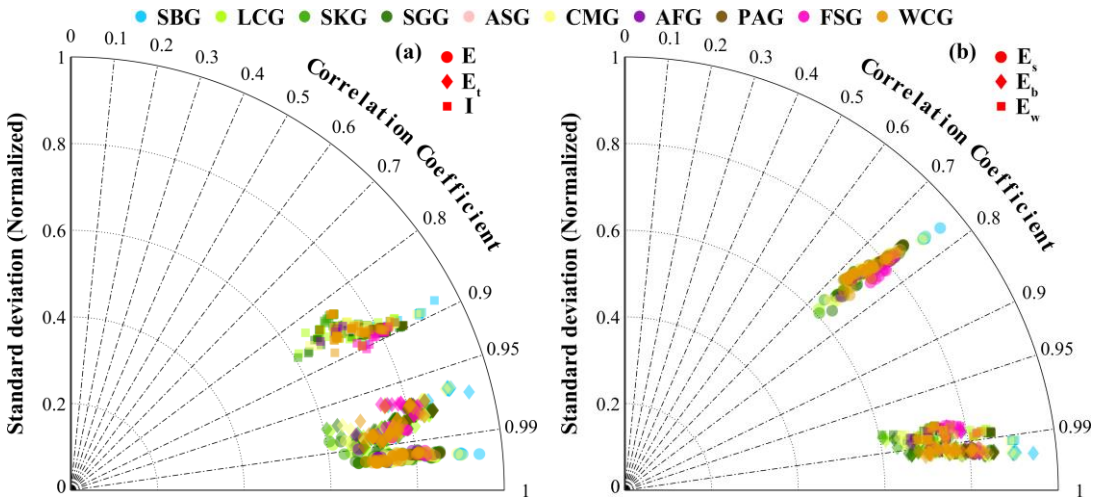

Figure 5. Taylor diagram comparing the MYEH-Eva module performance in the training stage for six types of evaporation for ten individual biomes. MYEH-Eva module: MY ecohydrology model evaporation module.

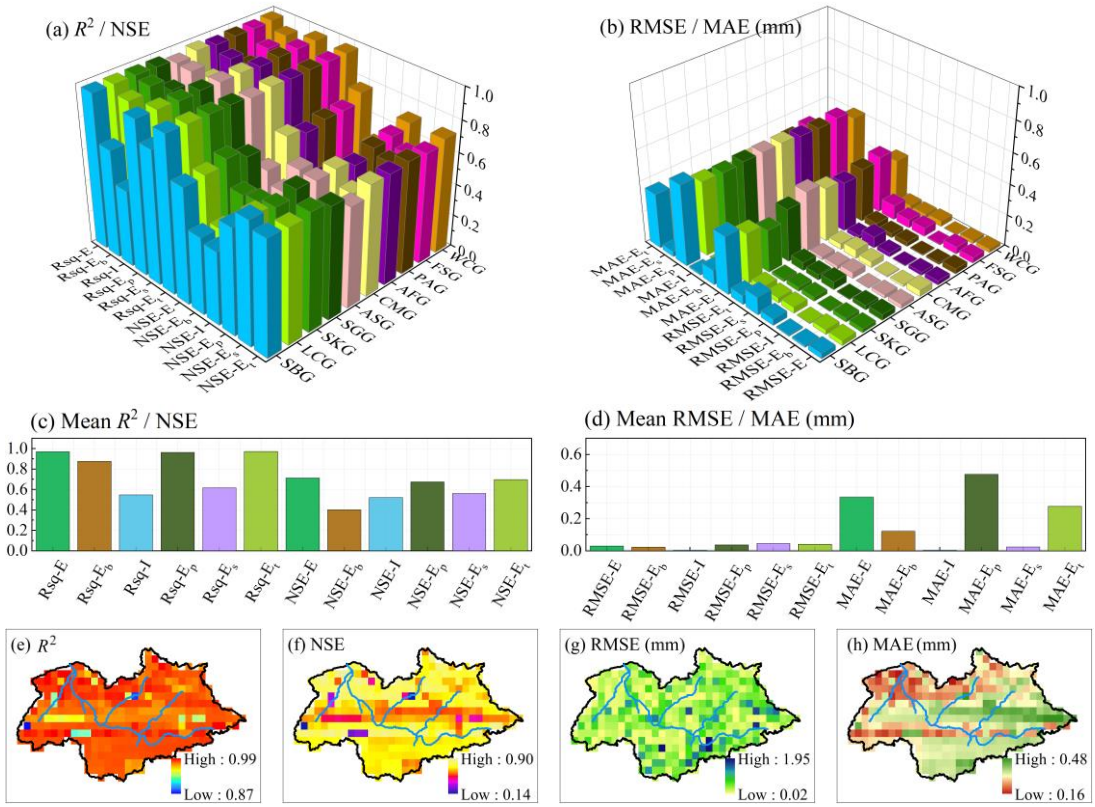

Figure 6. Results of the evaporation simulation with the MYEH-Eva module. (a–b) Accuracy and error of the evaporation simulation for ten individual biomes. (c–d) Mean precision and error of the simulation results for different evapotranspiration types. (e–h) Simulation results for the actual evaporation in the XRB. Statistical indicators: R^2 and Rsq: regression goodness of fit; NSE: Nash–Sutcliffe efficiency coefficient; RMSE: root-mean-square error; MAE: mean absolute error.

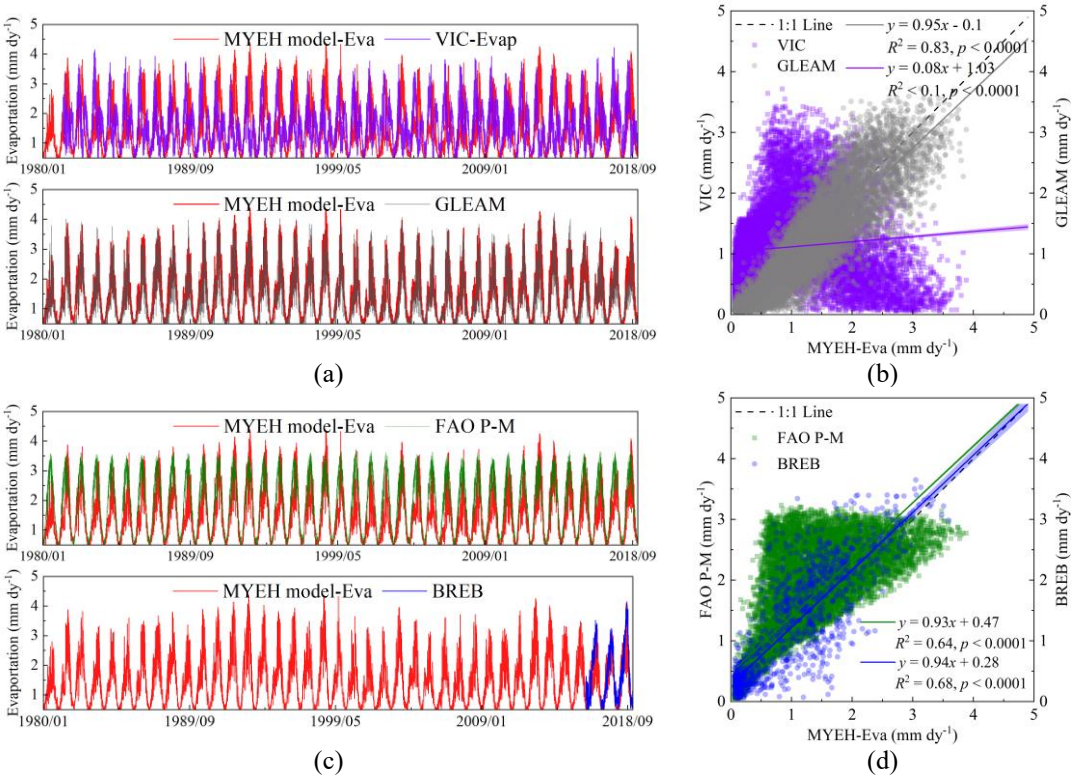

Figure 7. Comparison of the daily actual evaporation obtained with the MYEH-Eva module and four types of validation data from 1980 to 2018 in the XRB. The actual daily evaporation of the MYEH-Eva and BREB models were converted from 3-hour data. (a–b) Comparison between the values obtained from the Eva, VIC model, and GLEAM; (c–d) Comparison between the Eva module result and values obtained with the FAO Penman–Monteith (P–M) and BREB models. GLEAM: Global Land Evaporation Amsterdam Model; BREB: Bowen Ratio-Energy balance method.

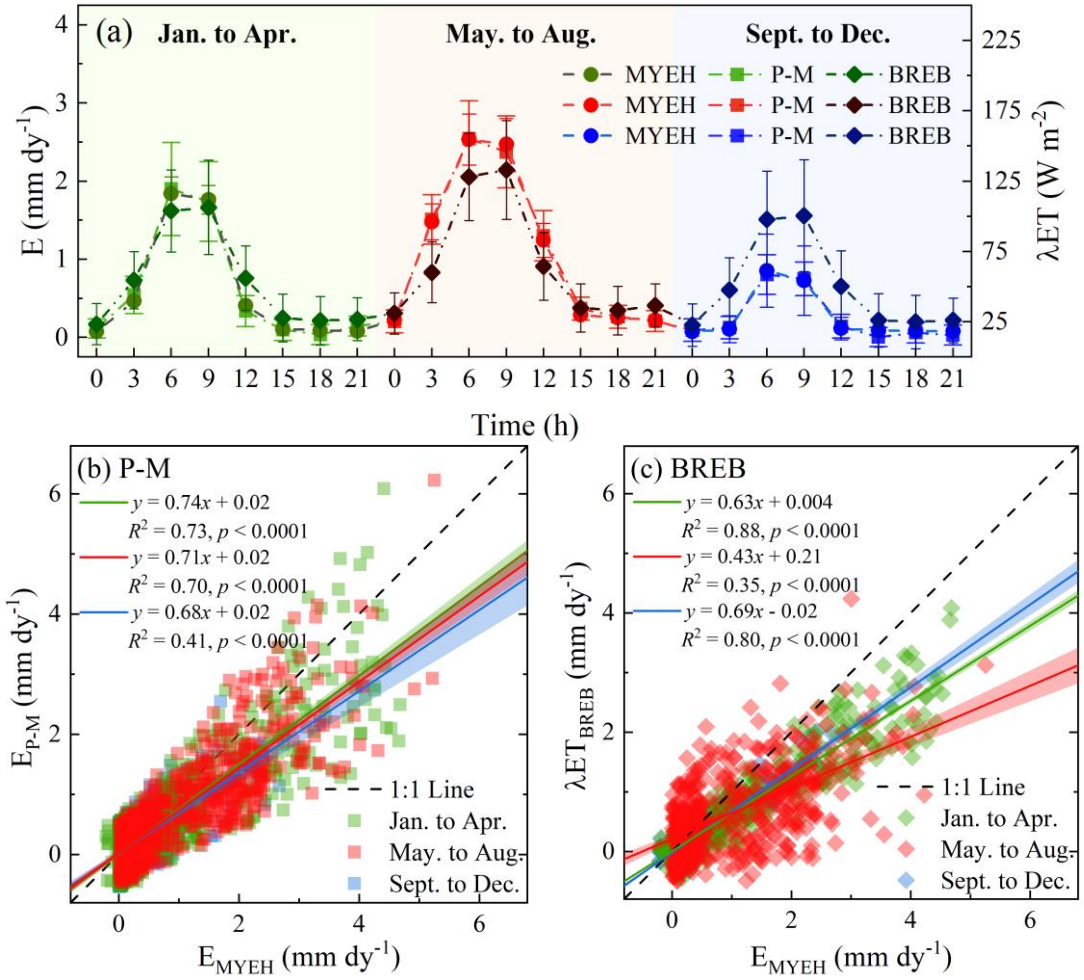

Figure 8. Comparison of the 3-hourly evapotranspiration simulated using three models, that is, the MYEH-Eva, P–M, and BREB models. The actual evaporation (E) in (a) was calculated with the MYEH-Eva and P–M models. The latent heat flux (λET) was calculated using the BREB model. Validation data used in this figure includes the period from October 2015 to October 2016.

Tables

Table 1. Characteristics of the datasets used for the downscaling evapotranspiration comparison.

Dataset	Spatial resolution	Version	Date used in study	Number of Data (Temporal resolution)
CMFD	0.1° to 0.05°	01.05.0016	1980.01.01-2018.12.31	335*14245*7 (1-day); 335*113960*7 (3-hour)
GLEAM	0.25° to 0.05°	V3.5a	1980.01.01-2018.12.31	335*14245*10 (1-day)
GSDE	0.083333° to 0.05°	2014	-	335*9 (-)
FVC	0.05°	V40	1981.01-2018.12	335*1748*1 (8-day)
LAI	0.05°	V50	1981.01-2018.12	335*1748*1 (8-day)
NPP	0.05°	V50	1982.01-2018.12	335*1702*1 (8-day)
Albedo	0.05°	V42	1981.01-2018.12	335*1748*6 (8-day)

Note: CMFD: China meteorological forcing dataset, in which the temperature, pressure, specific humidity, wind speed, downward shortwave radiation, downward longwave radiation, and precipitation rate data are used in the study. GLEAM: Global Land Evaporation Amsterdam Model (Martens et al. 2017), in which the actual evaporation, soil evaporation, interception loss, potential evaporation, snow sublimation, transpiration, open-water evaporation, root-zone soil moisture, surface soil moisture data are used to validate in the study. GSDE: The Global Soil Dataset for Earth System Modeling, in which the soil particle size, bulk density, and volumetric water content at 10/33/1500 KPa are used in the study. FVC: Fractional Vegetation Coverage. LAI: Leaf area index. NPP: Net Primary Production. Albedo: Broadband Albedo, include three spectral ranges: total shortwave, visible and near-IR under actual atmospheric conditions (so-called blue-sky albedos). FVC, LAI, NPP, and Albedo data are all from The Global Land Surface Satellite (GLASS) Product. In the table, number of data = grid number × time sequence × variable number.

Table 2. Input and output variables of MYEH-Eva module evaporation simulation module during training stage.

Layer	Dataset	Symbol	Variable name	Unit	Dataset	Symbol	Variable name	Unit
Input	CMFD	a	Precipitation rate	mm hr^{-1}	GSDE	j_5	Volumetric water content at -10 kPa	%
		b	Temperature	K		j_6	Volumetric water content at -33 kPa	%
		c	Downward longwave radiation	W m^{-2}		j_7	Volumetric water content at -1500 kPa	%
		d	Downward shortwave radiation	W m^{-2}		j_8	organic carbon	of weight
		e	Specific humidity	kg kg^{-1}	GLASS	k	FVC	%
		f	Wind speed	m s^{-1}		l	LAI	km^2 km^{-2}
		g	Pressure	Pa		m	NPP	kg km^{-2}
	GLEAM	h	Root-zone soil moisture	m^3 m^{-3}		i	VIS_BSA	-
		i	Surface soil moisture; 0-10	m^3 m^{-3}		n	VIS_WSA	-
	GSDE	j_1	Bulk density	g cm^{-3}		o	NIR_BSA	-
		j_2	Sand content	%		p	NIR_WSA	-
		j_3	Silt content	%		q	SW_BSA	-
		j_4	Clay content	%		r	SW_WSA	-
Output	GLEAM	E	Actual evaporation	mm dy^{-1}	GLEAM	E_s	Snow sublimation	mm dy^{-1}
		E_b	Bare-soil evaporation	mm dy^{-1}		E_t	Transpiration	mm dy^{-1}
		I	Interception loss	mm dy^{-1}		E_w	Open-water evaporation	mm dy^{-1}
		E_p	Potential evaporation	mm dy^{-1}				

Note: Due to the lack of temporal sequence of soil data, the model combines it into a group of variables to extract feature vectors for processing. VIS: Visible spectrum. NIR: Near-Infrared Reflectance. SW: Shortwave. BSA: Black sky albedo. WSA: White sky albedo.

Table 3. Weight values of the hidden, input, and output layers in the actual evaporation simulation of the MYEH-Eva module of semi-arid grassland.

Layer	x / y	w_{m1}	w_{m2}	w_{m3}	w_{m4}	w_{m5}	w_{m6}	w_{m7}	w_{m8}	w_{m9}	w_{m10}	w_{m11}	w_{m12}	w_{m13}	w_{m14}	w_{m15}
Input hidden	*a*	-3.57$^{\beta}$	7.32$^{\gamma}$	-8.79$^{\gamma}$	8.18$^{\alpha}$	-1.21$^{\delta}$	-4.32	5.30$^{\gamma}$	1.07	8.90$^{\gamma}$	-2.31	-1.19$^{\beta}$	-0.74	2.90$^{\beta}$	-1.69$^{\gamma}$	-3.55
	b	2.69$^{\gamma}$	-1.86$^{\gamma}$	-6.79$^{\beta}$	1.01$^{\alpha}$	2.88$^{\gamma}$	5.75	-3.01$^{\beta}$	-0.07	5.92$^{\gamma}$	2.72	-1.86$^{\alpha}$	0.86	-9.42$^{\gamma}$	-1.83$^{\gamma}$	0.56
	c	2.33$^{\gamma}$	-8.39$^{\gamma}$	-1.65$^{\gamma}$	-5.52$^{\alpha}$	-6.24$^{\gamma}$	1.21	2.76$^{\gamma}$	1.44	1.21$^{\delta}$	-6.55	-9.70$^{\alpha}$	4.17	3.75$^{\gamma}$	5.11$^{\gamma}$	-1.81
	d	-2.22$^{\gamma}$	-1.74$^{\delta}$	-6.70$^{\beta}$	-1.66$^{\beta}$	8.95$^{\gamma}$	6.81	8.57$^{\gamma}$	2.91	1.34$^{\delta}$	-5.99	-2.26$^{\alpha}$	4.55	2.38$^{\gamma}$	-2.63$^{\gamma}$	-1.49
	e	-6.49$^{\beta}$	1.34$^{\delta}$	-1.56$^{\beta}$	3.67$^{\alpha}$	6.60$^{\gamma}$	1.13	-7.29$^{\gamma}$	-1.06	5.48$^{\gamma}$	1.80	-3.46$^{\alpha}$	0.57	-5.21$^{\beta}$	-4.02$^{\beta}$	1.68
	f	-2.31$^{\gamma}$	-4.62$^{\gamma}$	1.69$^{\gamma}$	-8.98$^{\alpha}$	7.19$^{\gamma}$	-0.67	2.57$^{\gamma}$	-0.96	1.12$^{\gamma}$	1.99	-1.50$^{\alpha}$	-1.44	-1.82$^{\gamma}$	1.64$^{\gamma}$	1.73
	g	-5.35$^{\gamma}$	9.30$^{\gamma}$	5.54$^{\gamma}$	-7.41$^{\alpha}$	-2.22$^{\gamma}$	-0.41	-6.00$^{\gamma}$	0.82	9.71$^{\alpha}$	-0.42	1.09$^{\beta}$	0.47	4.10$^{\gamma}$	1.62$^{\delta}$	-0.49
	h	6.94$^{\gamma}$	1.90$^{\gamma}$	-1.38$^{\delta}$	1.39$^{\alpha}$	-1.20$^{\delta}$	-1.83	-1.12$^{\gamma}$	-0.74	1.09$^{\beta}$	1.08	2.88$^{\alpha}$	-2.95	7.68$^{\gamma}$	-9.92$^{\gamma}$	-0.35
	i	6.41$^{\gamma}$	2.18$^{\delta}$	-6.89$^{\gamma}$	1.26$^{\beta}$	-2.76$^{\delta}$	8.07	-8.44$^{\gamma}$	4.94	-2.20$^{\delta}$	-7.75	1.96$^{\alpha}$	1.37$^{\alpha}$	3.85$^{\gamma}$	-2.09$^{\delta}$	-6.44
	j	4.25$^{\gamma}$	-1.68$^{\gamma}$	-4.71$^{\gamma}$	4.35$^{\alpha}$	5.73$^{\gamma}$	0.65	4.30$^{\gamma}$	0.86	3.42$^{\gamma}$	-0.81	6.56$^{\alpha}$	0.47	9.96$^{\gamma}$	-1.19$^{\gamma}$	-1.41
	k	3.44$^{\gamma}$	6.11$^{\gamma}$	5.98$^{\beta}$	4.38$^{\alpha}$	8.33$^{\gamma}$	0.98	2.27$^{\gamma}$	1.39	-2.70$^{\gamma}$	-5.19	1.43$^{\beta}$	1.86	-1.09$^{\gamma}$	2.38$^{\gamma}$	0.86
	l	-1.58$^{\gamma}$	6.38$^{\gamma}$	3.33$^{\gamma}$	-3.46$^{\alpha}$	-3.19$^{\gamma}$	0.97	-5.04$^{\gamma}$	-0.45	3.25$^{\gamma}$	3.55	-1.98$^{\alpha}$	-1.29	-6.07$^{\gamma}$	3.23$^{\gamma}$	0.34
	m	8.18$^{\gamma}$	6.17$^{\gamma}$	-1.01$^{\delta}$	-5.45$^{\beta}$	1.42$^{\delta}$	-1.74$^{\alpha}$	4.70$^{\gamma}$	-4.55	2.10$^{\gamma}$	8.56	1.17$^{\beta}$	-1.61$^{\alpha}$	-2.83$^{\gamma}$	1.03$^{\gamma}$	6.63
	n	-8.99$^{\gamma}$	-6.13$^{\gamma}$	-2.51$^{\gamma}$	4.58$^{\beta}$	7.08$^{\gamma}$	0.51	6.24$^{\gamma}$	-2.17	7.42$^{\gamma}$	0.50	-5.85$^{\alpha}$	1.44$^{\alpha}$	6.64$^{\gamma}$	-3.40$^{\gamma}$	3.92
	o	1.03$^{\gamma}$	-3.29$^{\gamma}$	6.43$^{\beta}$	-2.16$^{\alpha}$	8.01$^{\gamma}$	-6.56	-1.29$^{\gamma}$	-1.64	-2.23$^{\gamma}$	9.16	-1.23$^{\beta}$	-3.64	1.37$^{\delta}$	2.09$^{\gamma}$	1.67$^{\alpha}$
	p	1.70$^{\beta}$	-1.76$^{\delta}$	-2.01$^{\gamma}$	-1.43$^{\alpha}$	2.83$^{\gamma}$	6.44	-6.61$^{\beta}$	1.12	-4.18$^{\gamma}$	-2.99	6.23$^{\alpha}$	-2.81$^{\alpha}$	-1.37$^{\gamma}$	2.09$^{\gamma}$	-4.29
	q	-7.33$^{\gamma}$	-1.62$^{\delta}$	3.73$^{\gamma}$	2.68$^{\beta}$	-4.75$^{\beta}$	5.64	1.38$^{\gamma}$	3.70	-5.43$^{\gamma}$	-2.10$^{\alpha}$	-1.61$^{\alpha}$	2.64$^{\alpha}$	1.06$^{\delta}$	3.20$^{\gamma}$	-1.78$^{\alpha}$
	r	5.10$^{\gamma}$	1.80$^{\delta}$	5.85$^{\gamma}$	-1.58$^{\beta}$	2.66$^{\gamma}$	5.23	1.70$^{\gamma}$	3.22	1.30$^{\gamma}$	2.44	-2.33	2.01	9.17$^{\beta}$	-2.82$^{\gamma}$	-6.04
Output hidden	*E*	-5.99$^{\alpha}$	-1.51	4.08	-3.66$^{\beta}$	-5.11	-4.72$^{\alpha}$	8.00	2.66	-2.67	6.90$^{\alpha}$	-1.59$^{\alpha}$	-4.27$^{\alpha}$	2.36	4.71$^{\alpha}$	4.04$^{\alpha}$

Note: In the table, w_{mi} (i represents 1 to 15) is used to connect or transfer information from the input layer to the hidden layer or from the hidden layer to the output layer; parameter m represents a to r and y, the input parameters and output parameters. α, β, γ, and δ represent model weight parameters multiplied by 10, 100, 1000 and 10000, respectively.

Table 4. Summary statistics for the performance of the MYEH-Eva module in the training and simulation stages for ten individual biomes in semi-arid grassland.

	Bias		R^2		Slope		NSE		RMSE		MAE		KGE	
	Tr.	Sim.	Tr.	Sim.	Tr.	Sim.	Tr.	Sim.	Tr.	Sim.	Tr.	Sim.	Tr.	Sim.
SBG	0.41	**0.27**[a]	0.88	**0.98**	0.87	**0.97**	**0.88**	0.72	**0.20**[b]	0.23[b]	**0.22**	0.37	0.17	**0.02**
LCG	0.36	**0.43**[a]	0.86	**0.98**	0.85	**0.97**	**0.86**	0.73	**0.15**[b]	0.19[b]	**0.21**	0.32	0.31	**0.02**
SKG	0.18	**0.24**[a]	0.87	**0.98**	0.86	**0.97**	**0.87**	0.77	**0.07**[b]	0.11[b]	**0.19**	0.27	0.37	**0.02**
SGG	0.33	**0.51**[a]	0.86	**0.98**	0.85	**0.97**	**0.85**	0.72	**0.25**[b]	0.25[b]	**0.22**	0.34	0.29	**0.02**
ASG	0.21	**0.29**[a]	0.86	**0.95**	0.85	**0.94**	**0.85**	0.57	**0.09**[b]	0.18[b]	**0.22**	0.39	0.34	**0.18**
CMG	0.29	**0.22**[a]	0.87	**0.98**	0.86	**0.97**	**0.87**	0.73	**0.11**[b]	0.27[b]	**0.22**	0.34	0.28	**0.05**
AFG	0.27	**0.42**[a]	0.87	**0.97**	0.86	**0.96**	**0.87**	0.69	**0.05**[b]	0.08[b]	**0.20**	0.32	0.33	**0.02**
PAG	0.44	**0.23**[a]	0.86	**0.97**	0.85	**0.96**	**0.86**	0.72	0.49[b]	**0.19**[b]	**0.23**	0.35	0.26	**0.02**
FSG	0.46	**0.85**[a]	0.84	**0.97**	0.83	**0.96**	**0.84**	0.72	**0.11**[b]	0.22[b]	**0.25**	0.37	0.24	**0.02**
WCG	0.26	**0.32**[a]	0.87	**0.98**	0.86	**0.97**	**0.87**	0.77	**0.07**[b]	0.11[b]	**0.19**	0.28	0.33	**0.03**

Note: Tr. and Sim. represent training stage and simulation stage. Statistical indicators: R^2: regression goodness of fit; NSE: Nash-Sutcliffe efficiency coefficient; RMSE: root-mean-square error; MAE, mean absolute error. RMSE and MAE are measured in mm dy^{-1}. The better value of each pair of values is boldfaced. [a] and [b] mean the statistics have the scale factor = 0.001 or 0.1.